The Relative Importance of Forced and Unforced Temperature Patterns in Driving the Time Variation of Low-Cloud Feedback

YUAN-JEN LIN,[a,b] GRÉGORY V. CESANA,[a,b] CRISTIAN PROISTOSESCU,[c] MARK D. ZELINKA,[d] AND KYLE C. ARMOUR[e]

[a] *Center for Climate Systems Research, Columbia University, New York, New York*
[b] *NASA Goddard Institute for Space Studies, New York, New York*
[c] *Department of Climate, Meteorology, and Atmospheric Sciences and Department of Earth Sciences and Environmental Change, University of Illinois Urbana–Champaign, Urbana, Illinois*
[d] *Lawrence Livermore National Laboratory, Livermore, California*
[e] *School of Oceanography and Department of Atmospheric Sciences, University of Washington, Seattle, Washington*

(Manuscript received 5 January 2024, in final form 26 September 2024, accepted 7 November 2024)

ABSTRACT: Atmospheric models forced with observed sea surface temperatures (SSTs) suggest a trend toward a more-stabilizing cloud feedback in recent decades, partly due to the surface cooling trend in the eastern Pacific (EP) and the warming trend in the western Pacific (WP). Here, we show model evidence that the low-cloud feedback has contributions from both forced and unforced feedback components and that its time variation arises in large part through changes in the relative importance of the two over time, rather than through variations in forced or unforced feedbacks themselves. Initial-condition large ensembles (LEs) suggest that the SST patterns are dominated by unforced variations for 30-yr windows ending prior to the 1980s. In general, unforced SSTs are representative of an ENSO-like pattern, which corresponds to weak low-level stability in the tropics and less-stabilizing low-cloud feedback. Since the 1980s, the forced signals have become stronger, outweighing the unforced signals for the 30-yr windows ending after the 2010s. Forced SSTs are characterized by relatively uniform warming with an enhancement in the WP, corresponding to a more-stabilizing low-cloud feedback in most cases. The time-evolving SST pattern due to this increasing importance of forced signals is the dominant contributor to the recent stabilizing shift of low-cloud feedback in the LEs. Using single-forcing LEs, we further find that if only greenhouse gases evolve with time, the transition to the domination of forced signals occurs 10–20 years earlier compared to the LEs with full forcings, which can be understood through the compensating effect between aerosols and greenhouse gases.

KEYWORDS: Sea surface temperature; Cloud radiative effects; General circulation models; Climate variability

1. Introduction

Projections of future warming in response to forcing depend on the magnitude of radiative feedbacks and, in particular, on how clouds will respond to changing climate conditions (Bony and Dufresne 2005; Sherwood et al. 2014; Forster et al. 2021). Previous research has shown that radiative feedbacks have considerable temporal variations (Andrews et al. 2015; Zhou et al. 2016; Andrews et al. 2018; Dong et al. 2020; Gregory et al. 2020; Rugenstein et al. 2020; Andrews et al. 2022), which adds to the uncertainty of climate prediction (Frey et al. 2017; Sherwood et al. 2020; Forster et al. 2021; Gjermundsen et al. 2021; Watanabe et al. 2021; Armour et al. 2024).

Radiative feedbacks vary over time in both the historical period (since around 1850) and future warming simulations. In most fully coupled atmosphere–ocean general circulation models (AOGCMs) where the atmospheric carbon dioxide (CO_2) concentration is abruptly quadrupled and kept constant for the rest of the simulation, the net radiative feedback becomes less stabilizing over time (i.e., a trend toward higher effective climate sensitivity) (Geoffroy et al. 2013; Andrews et al. 2015; Ceppi and Gregory 2017; Dong et al. 2020; Rugenstein et al. 2020). In the historical period, the feedback shows strong variability on decadal time scales. Most AOGCM historical simulations suggest a shift toward less-stabilizing net radiative feedback over the past few decades (Gregory et al. 2020; Dong et al. 2021; Salvi et al. 2023). However, atmospheric general circulation models (AGCMs) with prescribed observational SST and sea ice instead indicate a trend toward a more-stabilizing net radiative feedback (lower effective climate sensitivity) during the same time period (Zhou et al. 2016; Gregory and Andrews 2016; Andrews et al. 2018, 2022). The time evolution of net radiative feedback has been interpreted through changes in SST patterns, also referred to as the pattern effect (Stevens et al. 2016; Zhou et al. 2017; Dong et al. 2019). The divergent trends of net radiative feedback between the abovementioned AOGCM and AGCM simulations in recent decades can be explained by discrepancies between the modeled and observed SST patterns (Dong et al. 2021).

The potential for radiative feedbacks to vary over time as the SST pattern evolves can be interpreted in terms of a forced climate response. For instance, as is seen most clearly under an abrupt CO_2 doubling or quadrupling, SST patterns

Supplemental information related to this paper is available at the Journals Online website: https://doi.org/10.1175/JCLI-D-24-0014.s1.

Corresponding author: Yuan-Jen Lin, yl5278@columbia.edu

DOI: 10.1175/JCLI-D-24-0014.1

and thus radiative feedbacks vary as the ocean adjusts on a range of time scales (Held et al. 2010; Winton et al. 2010; Armour et al. 2013; Geoffroy et al. 2013; Rose et al. 2014; Rose and Rayborn 2016; Rugenstein et al. 2016; Lin et al. 2019, 2021; Eiselt and Graversen 2023). Moreover, non-CO_2 forcing agents, such as anthropogenic aerosols, Antarctic meltwater, or volcanic eruptions, can produce time-varying SST patterns and radiative feedbacks that are distinct from those from CO_2 forcing (Shindell 2014; Gregory et al. 2016; Marvel et al. 2016; Gregory et al. 2020; Dong et al. 2022; Günther et al. 2022; Salvi et al. 2023; Zhou et al. 2023). Another branch of literature has also shown that internal variability can influence radiative feedbacks through its influence on evolving SST patterns (Huber et al. 2014; Dessler et al. 2018; Gregory et al. 2020) and that, in general, the spatial patterns and magnitudes of radiative feedbacks under different modes of internal variability ("unforced feedbacks") are distinct from those induced by radiative forcing ("forced feedbacks") (Donohoe et al. 2014; Xie et al. 2016; Proistosescu et al. 2018; Dessler 2020; Wills et al. 2021; Uribe et al. 2022).

Here, we investigate another contribution to the time variation of radiative feedbacks. In light of the fact that forced and unforced feedbacks have different magnitudes, it is possible that a portion of net radiative feedback time evolution may stem from a changing relative importance of internal variability and forced response—rather than through variations in the magnitude of forced feedbacks or unforced feedbacks alone. For instance, early in the historical record when radiative forcing is small, we might expect the net radiative feedback to largely reflect feedbacks associated with internal variability. However, later in the historical record and in the future when radiative forcing is strong, we might expect the net radiative feedback to largely reflect feedbacks induced by the forcing. A key question is as follows: How important is such a shift in the relative importance of internal variability and forced response to the overall time variation of radiative feedbacks?

To answer the question, we begin by laying out a statistical framework to illustrate how forced and unforced variations combine to yield the net global radiative feedback (section 2). Results on the relative importance of the forced and unforced signals from initial-condition large ensembles are then shown. In section 3, we focus on the time evolution of low-cloud feedback and decompose the feedback change into components related to changes in forced response, changes in unforced variability, and changes in their relative importance. Section 4 highlights the role of the SST pattern effect in connecting the time-evolving SST pattern and low-cloud feedback. In section 5, we further explore how various forcing agents may interact to modify the relative importance of the forced and unforced variations. In section 6, we summarize our findings and discuss the broader implications of our research.

2. Relative importance of forced and unforced responses

a. Initial-condition large ensembles

To isolate the forced responses from the unforced internal variability, we used single-model, initial-condition large ensembles, including Community Earth System Model, version 2 (CESM2), large ensemble (Rodgers et al. 2021), Max Planck Institute Earth System Model version 1.1 (MPI-ESM1.1; Maher et al. 2019), and simulations from the National Aeronautics and Space Administration (NASA) Goddard Institute for Space Studies Model E2.1-G (GISS-E2.1-G; Kelley et al. 2020; Bauer et al. 2020; Miller et al. 2021). The initial-condition large ensembles aim to create a large number of simulations with identical forcing and slightly different atmospheric and/or oceanic initial conditions. By taking the ensemble mean, the relative contribution of internal variability is expected to weaken to $1/\sqrt{N}$, where N is the number of ensemble members (Gregory et al. 2020). Here, large ensembles from CESM2 ($N = 100$), MPI-ESM1.1 ($N = 100$), and GISS-E2.1-G ($N = 48$) all have relatively large N. Thus, any target field X in large ensemble simulations can be decomposed into two parts: 1) the ensemble-mean values of X (denoted as $\langle X \rangle$), which approximates the forced responses X_f, and 2) the anomalies relative to the ensemble mean of X (denoted as X^*), which approximates unforced variability X_u:

$$X = \langle X \rangle + X^*, \tag{1.1}$$

$$X_f \approx \langle X \rangle, \tag{1.2}$$

$$X_u \approx X^*. \tag{1.3}$$

b. Radiative feedback estimation

The evaluation of net radiative feedback often starts with the global-mean energy balance equation $N = F + R \approx F + \lambda T$ (Gregory et al. 2004), where N is the net downward radiation at the top of the atmosphere (TOA), F is the effective radiative forcing, and R represents the radiative responses (positive downward). The term R is often approximated as λT, where T indicates the global-mean surface temperature responses that act to dampen or amplify R through stabilizing or destabilizing feedback processes, denoted as λ. Here, the net radiative feedback λ is negative for a stable climate; thus, a more-negative (more-stabilizing) λ implies a less-sensitive climate.

In nonequilibrium climate states, such as for historical warming when the climate is still adjusting to forcing, λ is often quantified using the difference between two states, denoted as subscript $_1$ and $_2$ (Gregory et al. 2002; Dessler et al. 2018):

$$\lambda = \frac{(R_2 - R_1)}{(T_2 - T_1)} = \frac{(N_2 - N_1) - (F_2 - F_1)}{(T_2 - T_1)}. \tag{1.4}$$

At the same time, λ can be written in a differential form, where the derivatives can be estimated through linear regressions (Gregory et al. 2004; Rugenstein and Armour 2021):

$$\lambda = \frac{dR}{dT} = \frac{d(N - F)}{dT}. \tag{1.5}$$

c. Forced and unforced contributions to OLS regressions: Theory

The ordinary least squares (OLS) regression is widely used when examining the regression form of radiative feedback

(e.g., Sherwood et al. 2020). In a similar regression form, the SST pattern is usually calculated by regressing the map of regional SSTs against the global-mean values of surface temperature (e.g., Andrews et al. 2015). The use of OLS regression relies on the assumption that the independent variable (i.e., the x variable) is uncorrelated with the error term in the regression model, so the error term only considers unpredictable random error (i.e., the noise of the dependent variable). Thus, OLS regression estimates of radiative feedbacks may be biased when forced responses and unforced variability are tangled in both the independent variable (e.g., global-mean surface temperature) and the dependent variable (e.g., radiation). In the following text, we will quantify the relative contribution of forced and unforced signals to OLS regressions. We will also show how the two components jointly drive the time variation of SST patterns and radiative feedbacks.

Take the regression of a given field X against global-mean surface temperature T_g in a given historical time period, for example. Both the independent variable T_g and the dependent variable X consist of two parts that evolve with time: a forced response to net radiative forcing (from greenhouse gases, aerosols, volcanic eruptions, land use, etc.) and an unforced response related to internal variability. We can express the two components as follows:

$$T_g = T_{g,f} + T_{g,u}, \tag{1.6}$$

$$X = X_f + X_u, \tag{1.7}$$

where the subscripts $_f$ and $_u$ indicate the forced and unforced responses, respectively. By substituting the full response with the forced and unforced components, the regression-based estimate of dX/dT_g can be written as

$$\begin{aligned}\frac{dX}{dT_g} &= \frac{\mathrm{cov}(X, T_g)}{\mathrm{var}(T_g)} = \frac{\mathrm{cov}(X_f + X_u, T_{g,f} + T_{g,u})}{\mathrm{var}(T_{g,f} + T_{g,u})} \\ &= \frac{\mathrm{cov}(X_f, T_{g,f}) + \mathrm{cov}(X_f, T_{g,u}) + \mathrm{cov}(X_u, T_{g,f}) + \mathrm{cov}(X_u, T_{g,u})}{\mathrm{var}(T_{g,f}) + 2\,\mathrm{cov}(T_{g,f}, T_{g,u}) + \mathrm{var}(T_{g,u})},\end{aligned} \tag{1.8}$$

where $\mathrm{cov}(x, y)$ is the covariance between the variables x and y and $\mathrm{var}(x)$ is the variance of x. Both are estimated within a given time period (e.g., a 30-yr window). Since there is a general difference between the time evolution of forced and unforced responses, namely, the former is largely driven by radiative forcings and would be more linear within individual windows, whereas the latter consists of internal variations across different time scales (mainly interannual to decadal oscillations for a 30-yr window), we assume that the covariance between the forced and unforced responses is small. Equation (1.8) can then be expressed as

$$\frac{dX}{dT_g} = \frac{\mathrm{cov}(X_f, T_{g,f}) + \mathrm{cov}(X_u, T_{g,u})}{\mathrm{var}(T_{g,f}) + \mathrm{var}(T_{g,u})} + \sigma, \tag{1.9}$$

where the residual σ accounts for the combined effect from the three covariances between the forced and unforced responses, including $\mathrm{cov}(T_{g,f}, T_{g,u})$, $\mathrm{cov}(X_f, T_{g,u})$, and $\mathrm{cov}(X_u, T_{g,f})$. By rearranging Eq. (1.9), the regression estimate can be decomposed into forced and unforced regressions as follows:

$$\begin{aligned}\frac{dX}{dT_g} &= \frac{\mathrm{cov}(X_f, T_{g,f})}{\mathrm{var}(T_{g,f})}\frac{\mathrm{var}(T_{g,f})}{\mathrm{var}(T_{g,f}) + \mathrm{var}(T_{g,u})} + \frac{\mathrm{cov}(X_u, T_{g,u})}{\mathrm{var}(T_{g,u})} \\ &\quad \times \frac{\mathrm{var}(T_{g,u})}{\mathrm{var}(T_{g,f}) + \mathrm{var}(T_{g,u})} + \sigma \\ &= \frac{dX_f}{dT_{g,f}}\frac{\mathrm{var}(T_{g,f})}{\mathrm{var}(T_{g,f}) + \mathrm{var}(T_{g,u})} + \frac{dX_u}{dT_{g,u}}\frac{\mathrm{var}(T_{g,u})}{\mathrm{var}(T_{g,f}) + \mathrm{var}(T_{g,u})} \\ &\quad + \sigma\cdot\end{aligned} \tag{1.10}$$

Equation (1.10) suggests that the overall regression estimate is a linear combination of the forced and unforced regressions, with a specific weighting applied to each term. For forced regression $dX_f/dT_{g,f}$, it is multiplied by the ratio of forced T_g variance $\mathrm{var}(T_{g,f})$ to the sum of forced T_g variance and unforced T_g variance $[\mathrm{var}(T_{g,f}) + \mathrm{var}(T_{g,u})]$. Similarly, unforced regression $dX_u/dT_{g,u}$ is multiplied by the ratio of unforced T_g variance $\mathrm{var}(T_{g,u})$ to the sum of forced T_g variance and unforced T_g variance $[\mathrm{var}(T_{g,f}) + \mathrm{var}(T_{g,u})]$. We can simplify the equation further by writing it as

$$\frac{dX}{dT_g} = \frac{dX_f}{dT_{g,f}}r + \frac{dX_u}{dT_{g,u}}(1 - r) + \sigma, \tag{1.11}$$

$$r = \frac{\mathrm{var}(T_{g,f})}{\mathrm{var}(T_{g,f}) + \mathrm{var}(T_{g,u})}. \tag{1.12}$$

The ratio r and $(1 - r)$ indicate, respectively, the relative importance of forced and unforced temperature variances during the interval over which the regression has been performed. When r is small, the influence of forced regression on overall regression is weak, and the regression is largely determined by the unforced variability of X and T_g, and vice versa for large r. If X is taken to be the net TOA radiation R, the net radiative feedback can be written as a weighted sum of the feedback in response to forced variations and the feedback in response to unforced variations $\lambda = \lambda_f r + \lambda_u(1 - r) + \sigma$. Similarly, if X represents regional warming, then dX/dT_g becomes the net warming pattern over the time interval, and it will likewise be a weighted sum of forced and unforced components.

In summary, here we demonstrate how the forced and unforced signals jointly affect the strength of the OLS regression, which is widely used to calculate radiative feedback ($X = R$) and quantify SST patterns ($X = \text{SST}$). For each OLS regression, changes in either forced regression or unforced regression alter the strength of the overall regression. Even when both components are constant over time, changes in their relative importance [quantified as r and $(1 - r)$] could lead to time variation in the overall regression. Note that the residuals in this study are on average small (Fig. S2 in the online supplemental material), allowing for the separation of forced regression from unforced regression and suggesting a generally weak covariance between forced and unforced responses. For some individual ensemble members, the residuals are comparable to forced and unforced contributions, which should be interpreted with caution (Figs. 2 and 3).

d. *Forced and unforced contributions to OLS regressions: Model results*

Section 2c provides the theory of how the forced and unforced T_g variance determines their relative importance in OLS regressions. Figure 1 shows the model results that echo the theory. First, the forced and unforced T_g variances in the three LEs are shown (Figs. 1a–c). Note that to align closely with the meteorological cloud radiative kernels (Scott et al. 2020; Myers et al. 2021) that we will use in subsequent sections of the study, we define T_g as the area-weighted average of near-global (60°S–60°N) surface temperature over the ocean. This T_g definition is different from the commonly used global-mean surface temperature due to the exclusion of land and polar regions; however, we emphasize that the time evolution of the two is highly consistent (the correlation coefficient between the two T_g time series exceeds 0.97 in all ensemble members) and the different T_g definitions do not alter the conclusions (e.g., compare Fig. 1 with Fig. S1). Before the 1980s, all three LEs suggest a relatively mild forced warming (less than 0.4 K increase in the forced T_g since 1850; approximately less than 0.1 K for 30-yr intervals). After the 1980s, the forced T_g continues to increase, and its rate of increase also strengthens.

Figures 1d–f show the total, forced, and unforced T_g variances calculated in sliding 30-yr windows, where the x axis indicates the end year of each window. For 30-yr windows ending before 1980 (i.e., before the first vertical green line), the forced T_g variance is generally weaker than the unforced T_g variance. However, for windows ending after the 1980s, the forced T_g variance becomes stronger, while the unforced T_g variance remains of similar magnitudes. This different time evolution between forced and unforced T_g variances implies that forced responses have had more weight in OLS regressions since around the 1980s.

Indeed, the ratio r [defined in Eq. (1.12)], which quantifies the relative importance of forced signals, remains small for the 30-yr windows ending before 1980 (Figs. 1g–i). The averaged r before 1980 (i.e., the average over multiple windows) is 0.18 ± 0.02 in CESM2, 0.28 ± 0.03 in MPI-ESM1.1, and 0.15 ± 0.02 in GISS-E2.1-G, where the ensemble mean and one standard deviation (STD) across ensembles are shown. After 1980, r increases rapidly, in parallel with the rapid increase in greenhouse gases (GHG) emissions. The forced and unforced T_g variances are comparable between the end year of the 1990s and the end year of the early 2000s ($r \sim 0.5$). As $\text{var}(T_{g,f})$ continues to strengthen, $\text{var}(T_{g,f})$ generally outweighs $\text{var}(T_{g,u})$ in the late 2000s ($r > 0.5$) and has become more and more dominant since then. In GISS-E2.1-G, the overtake of forced signals in the 2000s is less obvious than in the other two large ensembles. Take the end year of 2010 (1981–2010 window), for example, $r = 0.72 \pm 0.06$ in CESM2, $r = 0.72 \pm 0.07$ in MPI-ESM1.1, and $r = 0.58 \pm 0.05$ in GISS-E2.1-G. Despite the weaker r in the 1981–2010 window in GISS-E2.1-G, all three models show a pronounced increase in r between the 1951–80 window and the 1981–2010 window (shown as the two vertical lines in Fig. 1; see the numbers in Table 1), suggesting an increasing dominance of forced signals in SST patterns and radiative feedbacks over the past few decades.

While r is generally weak before the end year of 1980, we note that there are local r maxima in all three models, which can be linked to major volcanic eruptions (Gregory et al. 2016). The first local maximum spans between the end year of 1890 and the end year of 1910 (i.e., the sliding 30-yr windows from 1861–90 to 1881–1910), arising from the volcanic eruption of Krakatau in 1883 and the Santa Maria eruption in 1902. The second local maximum exists around the end year of 1930 (1901–30 window), which includes the influences from both the 1902 Santa Maria eruption and the 1912 Novarupta/Katmai eruption. Another local maximum occurs around the end year of 1991, which can be related to the 1991 Pinatubo eruption. Furthermore, there is a local minimum around the end year of 1960, consistent with the decrease in major volcanic eruptions between 1920 and 1960.

3. Time-evolving low-cloud feedback

a. *Forced and unforced contributions to low-cloud feedback*

Previous research has suggested that the responses of low clouds are the primary source of intermodel spread in climate sensitivity estimates (Bony and Dufresne 2005; Caldwell et al. 2016; Zelinka et al. 2016; Forster et al. 2021) and that the time evolution of net radiative feedback is mostly driven by changes in cloud radiative feedback (e.g., Zhou et al. 2016). Therefore, here we focus on the time evolution of low-cloud radiative feedback by combining the annual-mean changes in SST and estimated inversion strength (EIS; Wood and Bretherton 2006) per unit warming with observation-based meteorological cloud radiative kernels (Scott et al. 2020; Myers et al. 2021), as illustrated below:

$$C_{\text{SST}} = \frac{\partial R}{\partial \text{SST}} \frac{d\text{SST}}{dT_g}, \tag{2.1}$$

$$C_{\text{EIS}} = \frac{\partial R}{\partial \text{EIS}} \frac{d\text{EIS}}{dT_g}. \tag{2.2}$$

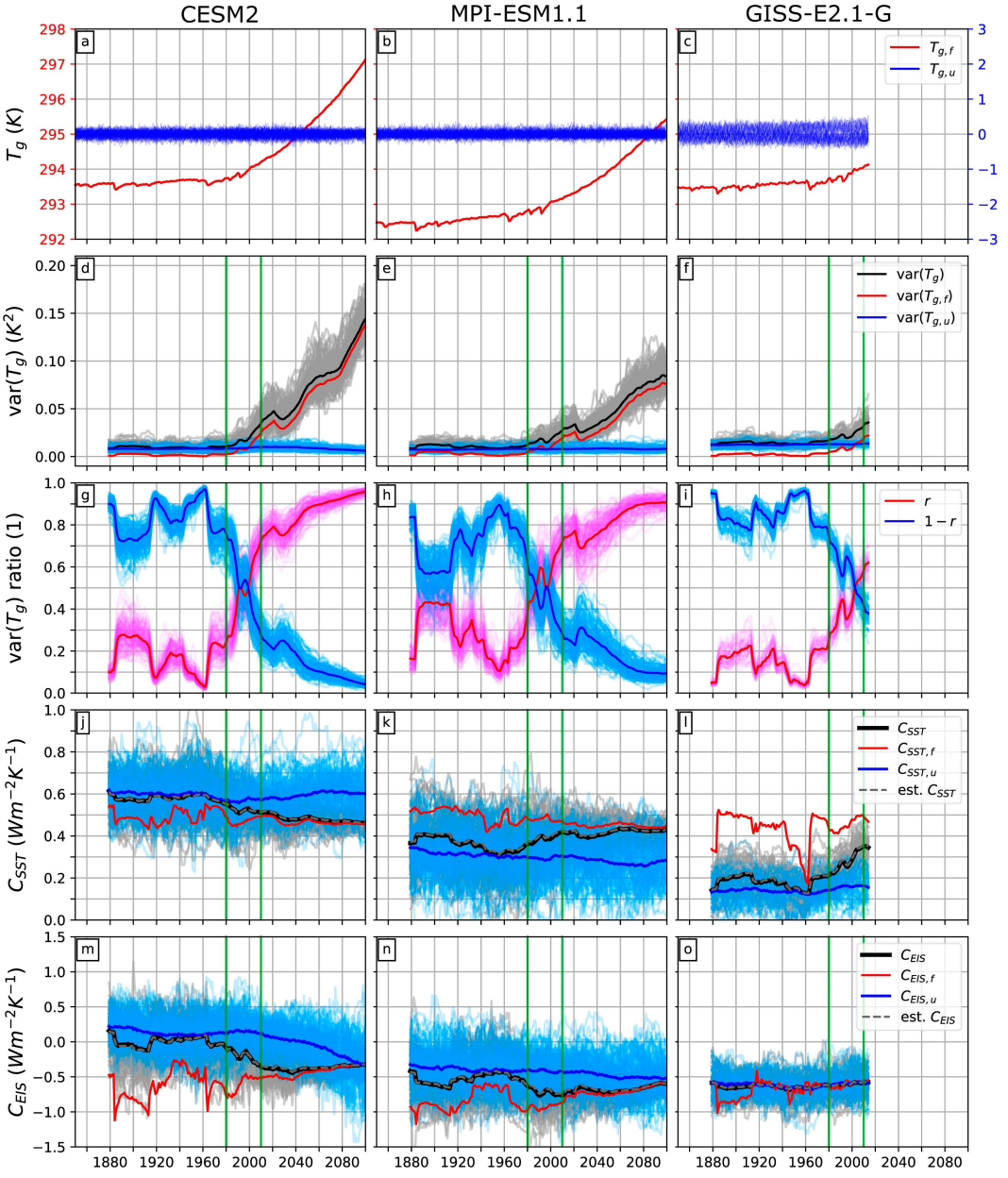

FIG. 1. Time evolution of forced (red; y axis on the left) and unforced (blue; y axis on the right) T_g in three initial-condition LEs: (a) CESM2, (b) MPI-ESM1.1, and (c) GISS-E2.1-G. Here, T_g is the area-weighted average of surface temperature within 60°S–60°N over the ocean. (d)–(f) Time evolution of the variance of T_g (black), $T_{g,f}$ (red), and $T_{g,u}$ (blue) in the three LEs. The variance is calculated on a sliding 30-yr window. (g)–(i) The ratio of the $T_{g,f}$ variance [red; r defined in Eq. (1.12)] and the ratio of the $T_{g,u}$ variance [blue; $(1-r)$] in the three LEs. (j)–(l) Time evolution of low-cloud feedback due to changes in full SST pattern C_{SST} (black), forced SST pattern $C_{\mathrm{SST},f}$ (red), and unforced SST pattern $C_{\mathrm{SST},u}$ (blue) in the three LEs. The term Est. C_{SST} (dashed gray) is calculated as the ensemble mean of $rC_{\mathrm{SST},f} + (1-r)C_{\mathrm{SST},u}$, meaning that the difference between the black and dashed gray lines is the residual term for ensemble mean. (m)–(o) As in (j)–(l), but for changes in the full EIS pattern C_{EIS} (black), forced EIS pattern $C_{\mathrm{EIS},f}$ (red), and unforced EIS pattern $C_{\mathrm{EIS},u}$ (blue). Note that the x axis marks the year in (a)–(c), while it denotes the end year of moving 30-yr windows in (d)–(o). Also, the range of y axis in C_{EIS} is three times larger than in C_{SST}. For each figure, dark-colored lines indicate the ensemble mean and light-colored lines show each ensemble member. The two vertical green lines in (d)–(o) mark the end years of 1980 and 2010, which, respectively, indicate the results from 1951–1980 and 1981–2010 windows that we focus on.

TABLE 1. Indices used to explain the time variation of low-cloud feedback C in the three initial-condition LEs. The term r is the ratio of the forced T_g variance [Eq. (1.12)]. The terms C_{SST} and C_{EIS} indicate the low-cloud feedbacks due to changes in SST and EIS patterns, and the subscripts $_f$ and $_u$ denote the forced and unforced components [Eqs. (2.1)–(2.4)]. The "average (avg)" in rows 3–8 indicates the average of multiple 30-yr sliding windows before the end year of 1980. Also, the IPWP warming ratio is calculated as the regional average of $d\mathrm{SST}/dT_g$ in the WP convective regions (30°S–30°N, 50°E–160°W) over the tropical average of $d\mathrm{SST}/dT_g$ (30°S–30°N). The pipe symbol | in this table is followed by the 30-yr window that is used to calculate the targeted field. Note that the forced components are calculated based on the ensemble-mean fields; thus, no spread across ensemble members is shown. For the total and unforced components, the ensemble-mean values and one STD across ensembles are shown.

	CESM2	MPI-ESM1.1	GISS-E2.1-G
$r\|_{1951–80}$ (1)	0.24 ± 0.07	0.38 ± 0.08	0.25 ± 0.04
$r\|_{1981–2010}$ (1)	0.72 ± 0.06	0.72 ± 0.07	0.58 ± 0.05
$C_{\mathrm{SST}}\mathrm{avg}\left(\frac{\mathrm{W}}{\mathrm{m^2\ K}}\right)$	0.57 ± 0.04	0.37 ± 0.04	0.20 ± 0.04
$C_{\mathrm{SST},f}\mathrm{avg}\left(\frac{\mathrm{W}}{\mathrm{m^2\ K}}\right)$	0.49	0.50	0.44
$C_{\mathrm{SST},u}\mathrm{avg}\left(\frac{\mathrm{W}}{\mathrm{m^2\ K}}\right)$	0.59 ± 0.04	0.31 ± 0.05	0.14 ± 0.04
$C_{\mathrm{EIS}}\mathrm{avg}\left(\frac{\mathrm{W}}{\mathrm{m^2\ K}}\right)$	−0.05 ± 0.10	−0.57 ± 0.10	−0.63 ± 0.08
$C_{\mathrm{EIS},f}\mathrm{avg}\left(\frac{\mathrm{W}}{\mathrm{m^2\ K}}\right)$	−0.62	−0.86	−0.68
$C_{\mathrm{EIS},u}\mathrm{avg}\left(\frac{\mathrm{W}}{\mathrm{m^2\ K}}\right)$	0.14 ± 0.10	−0.39 ± 0.11	−0.62 ± 0.08
$\mathrm{IPWP}\|_{1951–80}$ (1)	0.44 ± 0.11	0.82 ± 0.07	0.78 ± 0.05
$\mathrm{IPWP}_f\|_{1951–80}$ (1)	1.09	1.04	0.97
$\mathrm{IPWP}_u\|_{1951–80}$ (1)	0.30 ± 0.10	0.70 ± 0.07	0.73 ± 0.04
$\mathrm{IPWP}\|_{1981–2010}$ (1)	0.77 ± 0.10	0.96 ± 0.07	0.86 ± 0.05
$\mathrm{IPWP}_f\|_{1981–2010}$ (1)	1.03	1.09	1.03
$\mathrm{IPWP}_u\|_{1981–2010}$ (1)	0.32 ± 0.10	0.74 ± 0.08	0.71 ± 0.05
$\mathrm{IPWP}\|_{2070–99}$ (1)	0.97 ± 0.04	1.02 ± 0.04	—
$\mathrm{IPWP}_f\|_{2070–99}$ (1)	1.00	1.06	—
$\mathrm{IPWP}_u\|_{2070–99}$ (1)	0.47 ± 0.11	0.72 ± 0.07	—

The terms C_{SST} and C_{EIS} indicate the low-cloud radiative feedbacks due to changes in SST and EIS patterns, respectively. The terms $\partial R/\partial\mathrm{SST}$ and $\partial R/\partial\mathrm{EIS}$ are the meteorological cloud radiative kernels that quantify low-cloud radiative responses to local SST and EIS perturbations, developed by Scott et al. (2020). Note that the meteorological cloud radiative kernels are evaluated separately in four different observational datasets, including that from the Clouds and the Earth's Radiant Energy System Flux by Cloud Type (CERES-FBCT; Eitzen et al. 2017), the Moderate Resolution Imaging Spectroradiometer (MODIS; Platnick et al. 2015), the International Satellite Cloud Climatology Project (ISCCP; Young et al. 2018), and the Advanced Very High Resolution Radiometer Pathfinder Atmospheres–Extended (PATMOS-x) dataset (Heidinger et al. 2014). We adopt the average of four kernels due to their similar patterns and overall magnitudes (Scott et al. 2020; Myers et al. 2021). More importantly, since the meteorological cloud radiative kernels are time-invariant and model-independent, any time dependence of the low-cloud radiative feedback C analyzed here arises from the time evolution of SST or EIS patterns. The intermodel spread in C can also be fully attributed to the spread in SST or EIS patterns.

To evaluate the relative contributions from forced and unforced patterns of SST and EIS to the time-evolving C, we combine Eq. (1.11) with Eqs. (2.1) and (2.2):

$$C_{\mathrm{SST}} = \frac{\partial R}{\partial \mathrm{SST}}\left[\frac{d\mathrm{SST}_f}{dT_{g,f}}r + \frac{d\mathrm{SST}_u}{dT_{g,u}}(1-r) + \sigma\right] = C_{\mathrm{SST},f}r + C_{\mathrm{SST},u}(1-r) + \epsilon, \tag{2.3}$$

$$C_{\mathrm{EIS}} = \frac{\partial R}{\partial \mathrm{EIS}}\left[\frac{d\mathrm{EIS}_f}{dT_{g,f}}r + \frac{d\mathrm{EIS}_u}{dT_{g,u}}(1-r) + \sigma\right] = C_{\mathrm{EIS},f}r + C_{\mathrm{EIS},u}(1-r) + \epsilon, \tag{2.4}$$

where $C_{\mathrm{SST},f}$ is the forced component and $C_{\mathrm{SST},u}$ is the unforced component of the low-cloud feedback that arises from the local impact of the SST pattern. Both are global maps determined by annual-mean kernels and SST patterns. Similarly, $C_{\mathrm{EIS},f}$ and $C_{\mathrm{EIS},u}$ indicate the forced and unforced components of the EIS-related low-cloud feedback. The term ϵ represents the residual and is simply σ [Eq. (1.11)] multiplied by time-invariant meteorological cloud radiative kernels.

The main advantage of our low-cloud feedback evaluation is to isolate the influences of SST and EIS patterns on low-cloud feedback from other factors, such as the intermodel spread of time-evolving radiative forcing (Pincus et al. 2016) and the uncertainty of low-cloud radiative responses to SST and EIS perturbations. Moreover, using meteorological cloud radiative kernels, we have constrained observationally the dependence of low-cloud radiative effects on meteorology. However, the caveat is that the low-cloud feedback evaluated here could be different from the low-cloud feedback estimated exclusively in the models (i.e., allowing for model-specific coefficients), and the spread of low-cloud feedback among LEs contributes only in part to the overall intermodel spread of low-cloud feedback.

b. *Similarity and disparity among models*

Following Eqs. (2.3) and (2.4), here we review the time variation of low-cloud feedback from each AOGCM large ensemble and explain the shift in low-cloud feedback over the past few decades. First, most of the ensemble members in CESM2 suggest a trend toward more-negative C_{SST} and C_{EIS} between the end year of 1960 and the end year of 2010, with the EIS component having a stronger trend (black lines in Figs. 1j,m). Despite this negative trend in both C_{SST} and C_{EIS}, we can barely see the corresponding change in either forced component or unforced component. Instead, we find that the negative trend of C_{SST} and C_{EIS} is driven by changes in the relative importance of forced and unforced components. Between the end year of 1960 and the end year of 2010, there is

a transition from being dominated by unforced temperature variations (small r) to being dominated by forced temperature variations (large r; Fig. 1g). When unforced temperature variations dominate, the overall C is largely determined by its unforced component; thus, the two have similar magnitudes (closer blue and black lines when r is small). Similarly, when forced temperature variations dominate, the overall C is largely determined by the forced component (closer red and black lines when r is large). For both C_{SST} and C_{EIS}, since the unforced component is generally more positive than the forced component, the decreasing importance of unforced feedback (i.e., the increasing importance of forced feedback) in recent decades gives rise to a more-negative (more-stabilizing) low-cloud feedback during this time.

Similar explanations can be applied to MPI-ESM1.1 and GISS-E2.1-G. For example, if the unforced feedback component is more positive than the forced feedback component, such as C_{EIS} in CESM2 and MPI-ESM1.1 and C_{SST} in CESM2 (Table 1), the increasing importance of forced signals implies a negative trend of the overall low-cloud feedback (Figs. 1j,m,n). If the forced feedback component is more positive than the unforced feedback component (e.g., C_{SST} in MPI-ESM1.1 and GISS-E2.1-G; Table 1), the increasing importance of forced signals then implies a positive trend of the overall feedback (Figs. 1k,l). If, in the last case, the forced and unforced feedbacks have similar values (e.g., C_{EIS} in GISS-E2.1-G; Table 1), the overall feedback would barely change while r varies over time (Fig. 1o). For all three models, the ensemble-mean residual ϵ is negligible, shown as the difference between the gray dashed lines and the black lines in Figs. 1j–o.

By comparing the forced and unforced feedbacks among the three large ensembles, we also find that the intermodel spread of the C_{SST} and C_{EIS} arises mostly from the unforced component instead of the forced component. For SST contribution, $C_{\mathrm{SST},f}$ is 0.49, 0.50, and 0.44 W m^{-2} K^{-1} in CESM2, MPI-ESM1.1, and GISS-E2.1-G, respectively (row 4 of Table 1). However, $C_{\mathrm{SST},u}$ is 0.59 ± 0.04, 0.31 ± 0.05, and 0.14 ± 0.04 W m^{-2} K^{-1} at the same model order (row 5 of Table 1). As for the EIS contribution, the spread of unforced feedback is even larger to the extent that the sign is also uncertain. The term $C_{\mathrm{EIS},u}$ is positive (0.14 ± 0.10W m^{-2} K^{-1}) in CESM2, while it is negative in MPI-ESM1.1 and GISS-E2.1-G (−0.39 ± 0.11 and −0.62 ± 0.08 W m^{-2} K^{-1}, respectively; row 8 of Table 1). At the same time, the forced components have the same negative sign and similar magnitudes ($C_{\mathrm{EIS},f}$ = −0.62, −0.86, and −0.68 W m^{-2} K^{-1} in CESM2, MPI-ESM1.1, and GISS-E2.1-G, respectively; row 7 of Table 1).

c. *Attribution of time-evolving low-cloud feedback*

As shown in Eqs. (2.3) and (2.4), the temporal evolution of low-cloud feedbacks C_{SST} and C_{EIS} can be driven by three possible components: 1) changes in the forced low-cloud feedbacks $C_{\mathrm{SST},f}$ and $C_{\mathrm{EIS},f}$, 2) changes in the unforced low-cloud feedbacks $C_{\mathrm{SST},u}$ and $C_{\mathrm{EIS},u}$, and 3) changes in the relative importance between the forced and unforced signals, expressed as the ratio r [Eq. (1.12)]. Since the derivation for C_{SST} and C_{EIS} is identical, we will drop the subscripts and write the general form for low-cloud feedback as

$$C(t) = C_f(t)r(t) + C_u(t)[1 - r(t)] + \epsilon(t). \tag{2.5}$$

Here, t indicates a given 30-yr window used to calculate the feedback and the ratio. For the next 30-yr window, we can write the same form with $t = t + 1$. The change in C between the two adjacent 30-yr windows is then expressed as

$$\delta C(t) = \delta C_f(t)\overline{r(t)} + \delta C_u(t)[1 - \overline{r(t)}] + \delta r(t)[\overline{C_f(t)} - \overline{C_u(t)}] + \delta\epsilon(t), \tag{2.6}$$

where

$$\delta X(t) = X(t + 1) - X(t), \tag{2.7}$$

$$\overline{X(t)} = \frac{X(t + 1) + X(t)}{2}. \tag{2.8}$$

The term X can be C, C_f, C_u, or r. To attribute the C difference between the two nonadjacent windows, for example, the 30-yr windows of 1951–80 and 1981–2010, we can sum all the $\delta C(t)$ between the two:

$$\sum_{t=1951-1980}^{t=1980-2009} \delta C(t) = \sum_{t=1951-1980}^{t=1980-2009} \Big\{\delta C_f(t)\overline{r(t)} + \delta C_u(t)[1 - \overline{r(t)}] + \delta r(t)[\overline{C_f(t)} - \overline{C_u(t)}] + \delta\epsilon(t)\Big\}. \tag{2.9}$$

For clarity, we omit the time index and rewrite Eq. (2.9) into a more general form:

$$\Delta C = \sum \delta C_f \bar{r} + \sum \delta C_u(1 - \bar{r}) + \sum \delta r(\overline{C_f} - \overline{C_u}) + \Delta\epsilon. \tag{2.10}$$

The symbol Δ denotes the C difference given two windows and is simply the sum of all the differences from adjacent windows between the two. Using Eq. (2.10), we attribute the change in low-cloud feedback between any two windows to the contribution of forced feedback changes (the first term on the rhs), followed by the contribution of unforced feedback changes and the contribution of the ratio changes (the second and third terms on the rhs). The term $\Delta\epsilon$ again indicates the residual, which is associated with the combined effects from the covariance between forced and unforced signals (see section 2c for more details).

1) HISTORICAL PERIOD

Figure 2 shows the ΔC decomposition between the 30-yr windows of 1951–80 and 1981–2010. In both CESM2 and MPI-ESM1.1, ΔC_{EIS} is stronger than ΔC_{SST} and suggests a negative shift of low-cloud feedback during this period, consistent with Fig. 1. The decomposition also reveals that the change in r is the primary reason for the negative shift of C_{EIS}, shown as strong negative values of the "ratio" term. In CESM2, all ensemble members agree that the increasing importance of the forced signals (increasing r) leads to negative

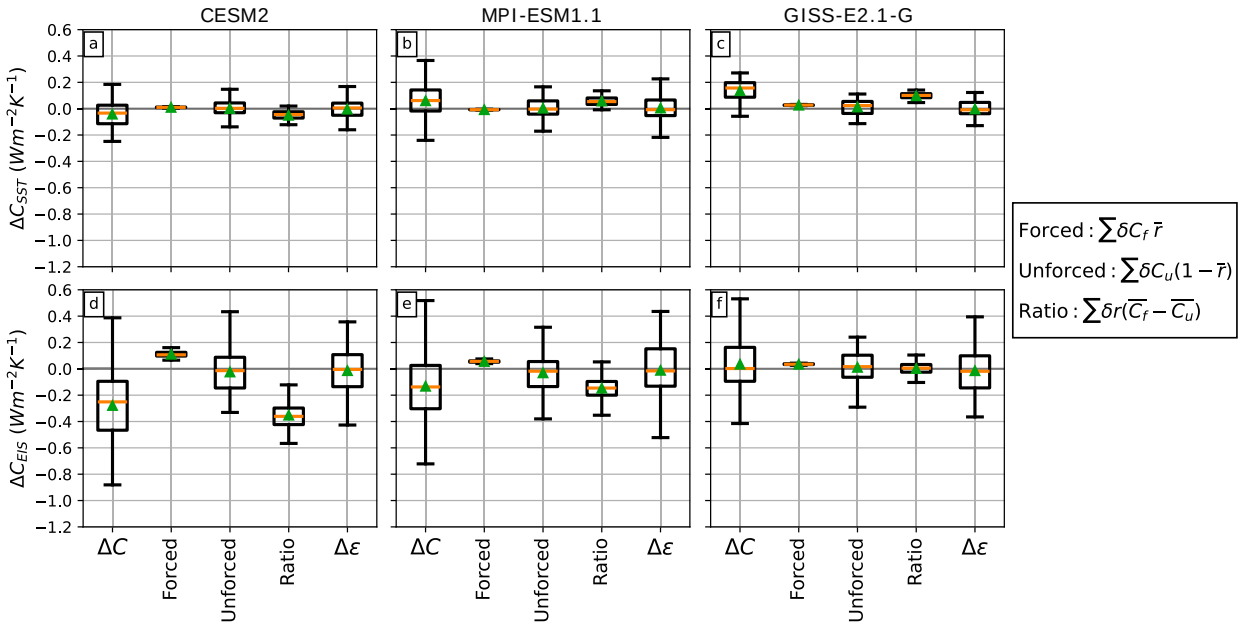

FIG. 2. Decomposition of ΔC_{SST} between the 30-yr windows of 1951–80 and 1981–2010 in (a) CESM2, (b) MPI-ESM1.1, and (c) GISS-E2.1-G. (d)–(f) As in (a)–(c), but for ΔC_{EIS}. The terms forced, unforced, and ratio represent the contributions from changes in forced feedback, changes in unforced feedback, and changes in r (the relative importance between the forced and unforced feedbacks), respectively. The term $\Delta\epsilon$ is the residual term. The calculation of each component follows Eq. (2.10) and is shown in the legend. In each box plot, the orange line indicates the median and the green triangle indicates the ensemble mean.

ΔC_{EIS} (Fig. 2d). More than 75% of the ensemble members in MPI-ESM1.1 agree with the above result (Fig. 2e). Meanwhile, the change in the forced component gives rise to a small increase in low-cloud feedback (the "forced" term). The influence of the unforced feedback change varies among ensembles and has no robust contribution to ΔC in recent decades (the "unforced" term). In GISS-E2.1-G, the ratio term contributes to the weak positive shift of C_{SST} (Fig. 2c). As for ΔC_{EIS}, the strength of the forced and unforced components is similar; therefore, the contribution of Δr is weak and insignificant (Fig. 2f).

By decomposing the low-cloud feedback change between 1951–80 and 1981–2010, we summarize that the increasing importance of forced signals (increasing r) is the main cause for the shift in low-cloud feedback over the past few decades in CESM2 and MPI-ESM1.1 large ensembles.

2) FUTURE WARMING SCENARIOS

In addition to the shift in low-cloud feedback C over the past few decades, we notice that C also evolves with time in future warming projections. In general, we find that C_{EIS} becomes more positive (less stabilizing) throughout the century in the SSP370 simulations of CESM2 and the RCP8.5 simulations of MPI-ESM1.1, while the change in C_{SST} is relatively weak (Fig. 1). The result is consistent with previous studies suggesting a less-stabilizing net radiative feedback over time due to EIS changes in CO_2-increasing simulations (Rose and Rayborn 2016; Ceppi and Gregory 2017, 2019; Dong et al. 2020; Lin et al. 2021).

To quantify and attribute the change in C_{EIS}, we decompose ΔC_{EIS} between the current climate (i.e., 1981–2010) and the projected climate at the end of the century (i.e., 2070–99; Fig. 3). More than 50% of ensemble members from CESM2 and more than 75% of ensemble members from MPI-ESM1.1 show positive ΔC_{EIS} in response to future warming. More importantly, this long-term positive change in C_{EIS} arises mainly from changes in the forced component, shown as strong positive values of the forced term (Figs. 3c,d). Changes in either the unforced component (unforced) or the relative importance between forced and unforced signals (the "ratio" term) instead lead to a more-negative C_{EIS} for most of the ensemble members.

4. The role of SST pattern effect

a. Overview

We showed above how the time variation of low-cloud feedbacks C_{SST} and C_{EIS} depends on changes in SST and EIS regressions, including their forced and unforced components. To build a physical understanding that connects the two, we compare the time-evolving SST and EIS regressions among the three large ensembles (Figs. 4 and 5) and highlight the role of SST pattern effect in setting the time-evolving C. Here, the SST pattern effect generally refers to the differences in radiative anomalies (between models or over different time periods) that can be attributed to variations in surface warming patterns (Stevens et al. 2016; Zhou et al. 2017; Dong et al. 2019). The spatial patterns $d\text{SST}/dT_g$ and $d\text{EIS}/dT_g$ are obtained by regressing local SST and EIS onto global-mean temperature change and separating into forced and unforced components following Eq. (1.11).

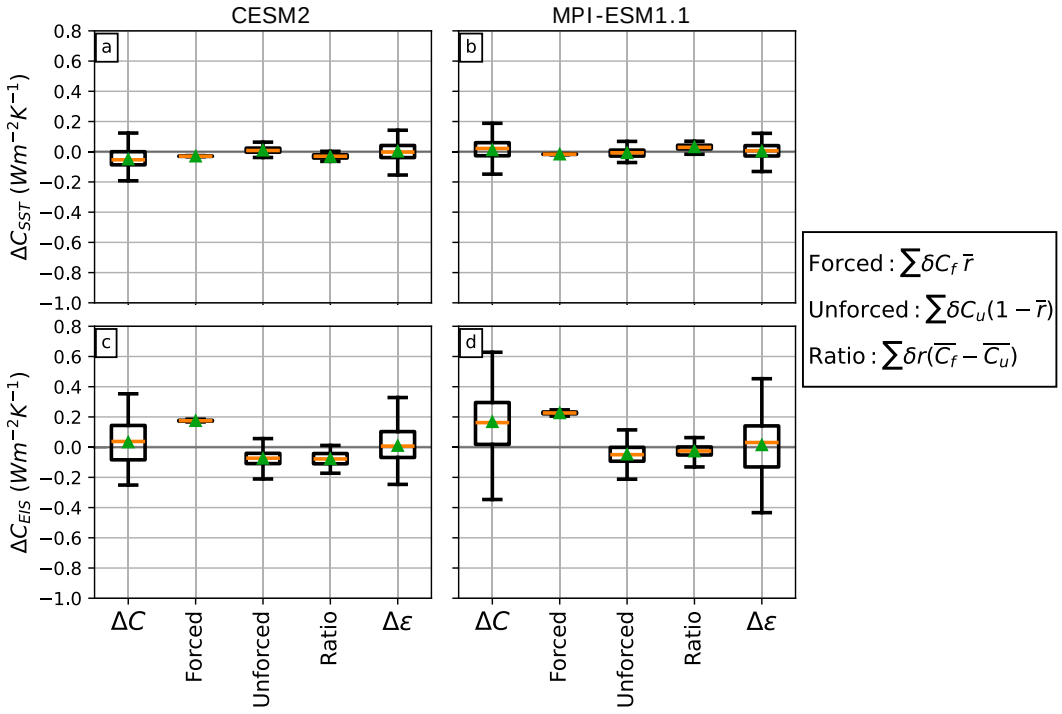

FIG. 3. As in Fig. 2, but for the ΔC_{SST} decomposition between the 30-yr windows of 1981–2010 and 2070–99 in (a) CESM2 and (b) MPI-ESM1.1 and for the ΔC_{EIS} decomposition between the 30-yr windows of 1981–2010 and 2070–99 in (c) CESM2 and (d) MPI-ESM1.1.

For all three large ensembles, the overall SST pattern $d\mathrm{SST}/dT_g$ (first column of Fig. 4) is determined by both the forced component $d\mathrm{SST}_f/dT_{g,f}$ (second column) and the unforced component $d\mathrm{SST}_u/dT_{g,u}$ (third column), depending on their relative importance indicated by r (Fig. 1; Table 1). The residual σ (fourth column of Fig. 4) remains small throughout different time periods, again indicating that the assumption made in section 2c is valid. The forced SST pattern characterizes a more uniform warming per unit increase in $T_{g,f}$, while the unforced SST pattern is more heterogeneous per unit change in $T_{g,u}$. All three models commonly show this fundamental difference between the forced and unforced SST patterns from the preindustrial era to the end of the twenty-first century.

b. *Historical period*

Within the large ensembles, the unforced SST pattern is similar to the SST anomalies from the prevailing climate variability in interannual time scales—El Niño–Southern Oscillation (ENSO), which we first illustrate for CESM2. Per unit increase in unforced T_g, there is an enhanced surface warming in the eastern Pacific (EP) and surface cooling in the western Pacific (WP) [Fig. 4a(3)]. Due to the small r in the 30-yr window of 1951–80 ($r = 0.24 \pm 0.07$), the overall SST pattern $d\mathrm{SST}/dT_g$ also reflects ENSO-like SST features [Fig. 4a(1)], while the influence of the forced SST pattern is notably weak [Fig. 4a(2); see Fig. S3 with the relative importance multiplied]. The surface cooling in the WP convective regions leads to an overall cooling in the free troposphere in the tropics, which destabilizes the low-level troposphere (e.g., Mauritsen 2016; Andrews and Webb 2018). The destabilization is particularly strong in the EP because of the substantial contrast between free-tropospheric cooling and surface-enhanced warming [Figs. 5a(1) and 5a(3)]. This low-level destabilization acts to decrease the marine stratocumulus cloud over the EP (Wood and Bretherton 2006), accounting for more-positive low-cloud feedback during this time.

In the 30-yr window of 1981–2010, on the other hand, the overall SST pattern is strongly affected by the forced signals ($r = 0.72 \pm 0.06$). Compared to the unforced SST pattern, the forced SST pattern is more spatially uniform, with slightly enhanced warming in the Northern Hemisphere (NH) and reduced warming in the Southern Hemisphere (SH). The surface warming in the WP convective regions is also stronger than that in the EP stratocumulus cloud regions [Fig. 4b(2)]. As a result, the overall SST pattern in 1981–2010 is less ENSO-like [Fig. 4b(1)] compared to that in 1951–80 [Fig. 4a(1)]. Correspondingly, per unit increase in T_g, the low-level troposphere in the EP shifts from being strongly unstable in 1951–80 [Fig. 5a(1)] to becoming slightly unstable in 1981–2010 [Fig. 5b(1)]. The 1981–2010 meteorological condition favors low-cloud formation and more-stabilizing low-cloud feedback in comparison with that in 1951–80.

The abovementioned mechanism applies to all three LEs, highlighting the distinct forced and unforced SST patterns that jointly shape the overall SST pattern with time-dependent weighting r for each component. We particularly focus on the warming contrast between the WP and the EP, which explains the time variation of low-cloud feedback through modifying low-level

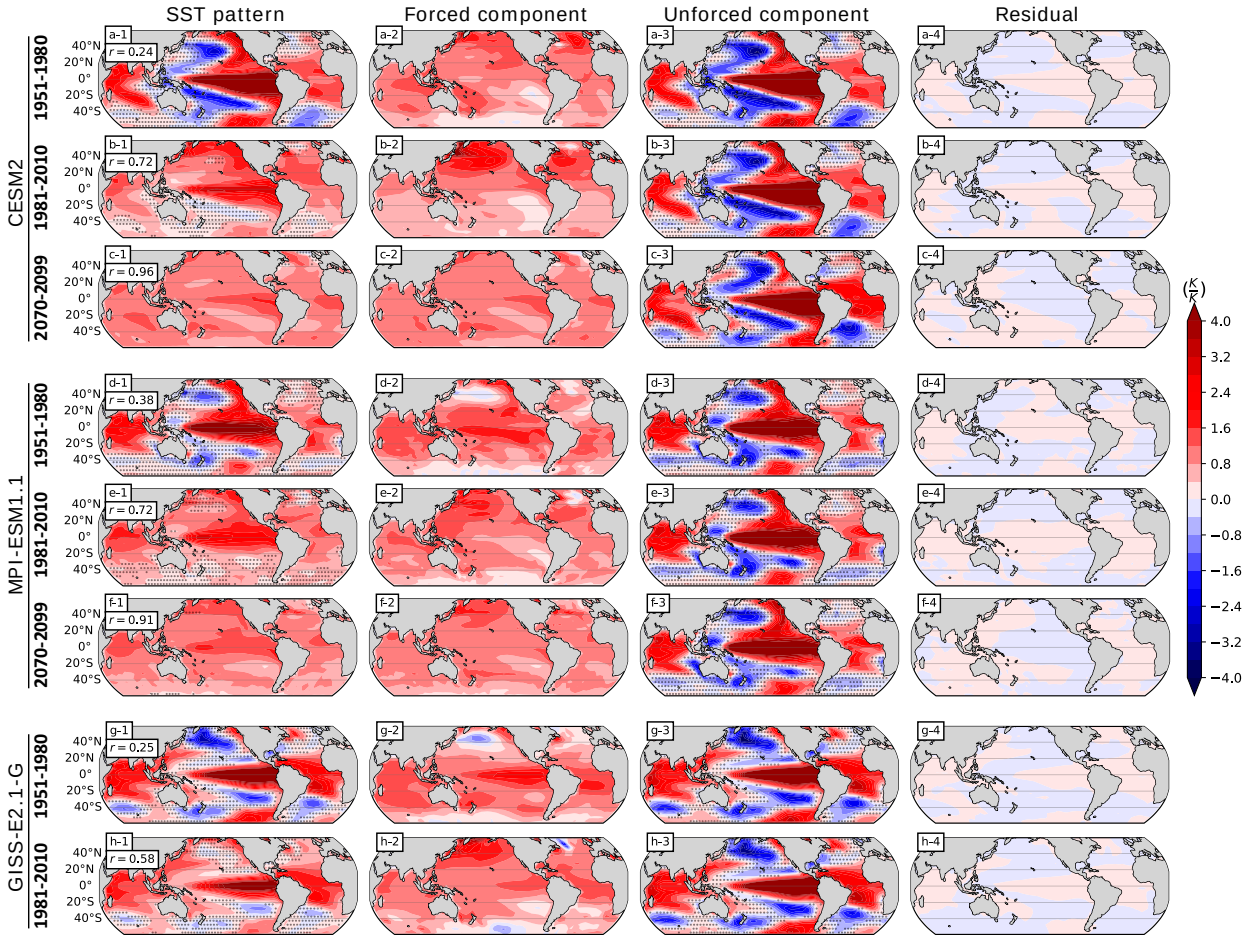

FIG. 4. (from left to right) Overall SST pattern dT/dT_g, the forced component $dT_f/dT_{g,f}$, the unforced component $dT_u/dT_{g,u}$, and the residual term σ calculated from different 30-yr windows in the three AOGCM LEs. For each panel, the 30-yr window and the LEs used are labeled on the left. In the overall and unforced SST patterns, contours indicate the ensemble mean and stippling indicates the regions where the one STD calculated across ensembles is larger than the ensemble-mean values. For the forced SST pattern, no stippling is shown since it is calculated based on the ensemble-mean fields before applying the OLS regression.

stability (C_{EIS}), while C_{SST} that quantifies local SST impacts plays a minor role in adjusting the C variations in recent decades. To further quantify this radiatively essential SST pattern, we define the Indo-Pacific warm pool (IPWP) warming ratio as the regional average of $d\mathrm{SST}/dT_g$ in the western Pacific convective regions (30°S–30°N, 50°E–160°W) over the tropical average of $d\mathrm{SST}/dT_g$ (30°S–30°N), consistent with the quantification proposed in Dong et al. (2019) and Wills et al. (2022).

In CESM2, the IPWP index becomes larger from 0.44 ± 0.11 in 1951–80 to 0.77 ± 0.10 in 1981–2010 (Table 1), associated with a more-stabilizing low-cloud feedback. The increased IPWP index can be explained by the increase in r, along with small unforced IPWP indices and large forced IPWP indices. In MPI-ESM1.1 and GISS-E2.1-G, we also observe an increase in the IPWP index but both with weaker magnitudes (Table 1). Given the similar time evolution of r among models and the large intermodel spread of unforced C_{EIS}, we propose that the intermodel spread of IPWP time evolution arises mostly from the unforced IPWP index.

Indeed, all three models produce similar forced IPWP indices, ranging from 0.97 to 1.09 in 1951–80 and 1.03 to 1.09 in 1981–2010. The close-to-unity values in both time periods indicate that the WP warming is similar to the overall warming in the tropics (i.e., spatially uniform forced SST responses). However, the unforced IPWP index varies widely among models. In 1951–80, IPWP_u is 0.30 ± 0.10 in CESM2, associated with the ENSO-like unforced SST pattern in which surface cooling occurs in the WP convective regions [Fig. 4a(3)]. Meanwhile, this WP cooling is much more limited and weaker in MPI-ESM1.1 despite the model still projecting an ENSO-like unforced SST pattern [Fig. 4d(3)]. In GISS-E2.1-G, there is barely any cooling in the WP convective regions. Surface warming is strong in both the tropical WP and EP regions [Fig. 4g(3)]. This weak-to-no cooling in the WP region would correspond to a higher IPWP index in both models (0.70 ± 0.07 in MPI-ESM1.1 and 0.73 ± 0.04 in GISS-E2.1-G) in 1951–80, limiting the IPWP increase in 1981–2010 when forced signals have become more dominant. In summary, the

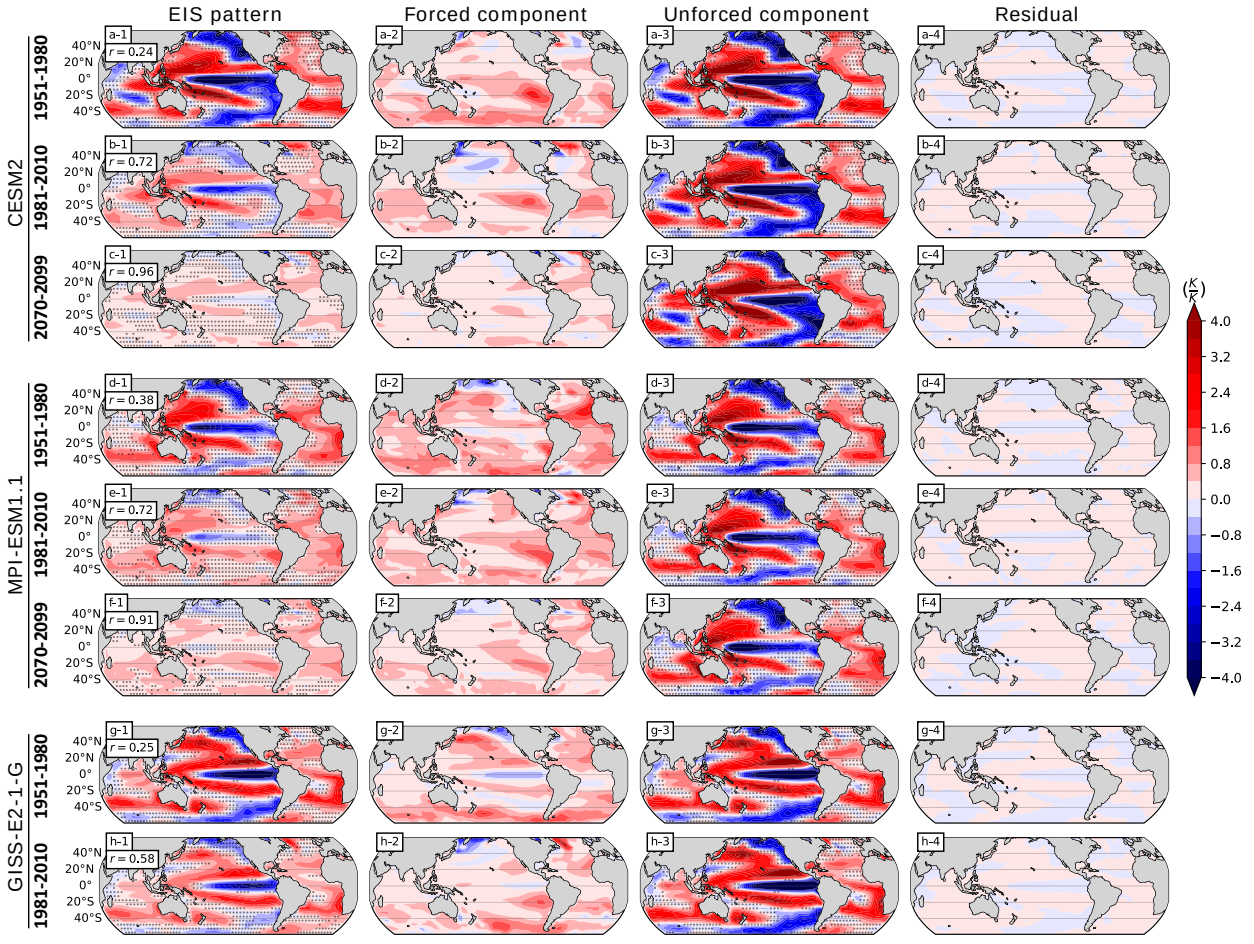

FIG. 5. As in Fig. 4, but for the overall EIS pattern $d\mathrm{EIS}/dT_g$, the forced component $d\mathrm{EIS}_f/dT_{g,f}$, the unforced component $d\mathrm{EIS}_u/dT_{g,u}$, and the residual term σ calculated from each 30-yr window in each AOGCM LEs.

large intermodel spread of unforced WP relative warming IPWP_u echoes the large spread of unforced $C_{\mathrm{EIS},u}$ (Fig. 1), which is responsible not only for the intermodel spread of C_{EIS} but also for the diverse time evolution of C_{EIS} among models.

c. *Future warming scenarios*

The relative importance of the forced response r outweighs the unforced variability for the 30-yr window ending around the 2010s and becomes increasingly dominant over time since then. At the end of the twenty-first century, r reaches 0.85–0.95, depending on the models and warming scenarios (Fig. 1). Comparing the SST patterns between the windows of 1981–2010 and 2070–99, we find that the changes in the overall SST pattern arise mostly from the changes in the forced component, except that some of the tropical regions are still influenced by unforced variability in the earlier period. The result is expected since r has been large, indicating a weak influence from the unforced variability. The change in forced SST pattern features delayed warming in the southeastern Pacific and the Southern Ocean [comparing Fig. 4b(2) and Fig. 4c(2) for CESM2; Fig. 4e(2) and Fig. 4f(2) for MPI-ESM1.1], corresponding to a decrease in the forced IPWP index (from 1.03 to 1.00 in CESM2; 1.09 to 1.06 in MPI-ESM1.1). The change in the SST pattern in turn leads to a less-positive EIS in the southeastern Pacific [comparing Fig. 5b(2) and Fig. 5c(2) for CESM2; Fig. 5e(2) and Fig. 5f(2) for MPI-ESM1.1] and a less-stabilizing C_{EIS}. The time-evolving SST and EIS patterns explain the forced contribution to the positive ΔC_{EIS} shown in Fig. 3, highlighting the role of the pattern effect.

Despite the weak influence of unforced variability on overall C in future projections (small r), there is a negative trend of unforced C_{EIS} in CESM2 (Fig. 1m), which can also be understood through the pattern effect. During the 1981–2010 window, the strong ENSO-like unforced SST pattern [Fig. 4b(3)] corresponds to a small IPWP_u (0.32 ± 0.10; Table 1). However, the WP warming becomes stronger near the end of the century [Fig. 4c(3)], corresponding to a higher IPWP_u index (0.47 ± 0.11; Table 1) and a more-negative unforced C_{EIS}. The reasons for the time evolution of the unforced SST pattern are beyond the scope of this study and require further research.

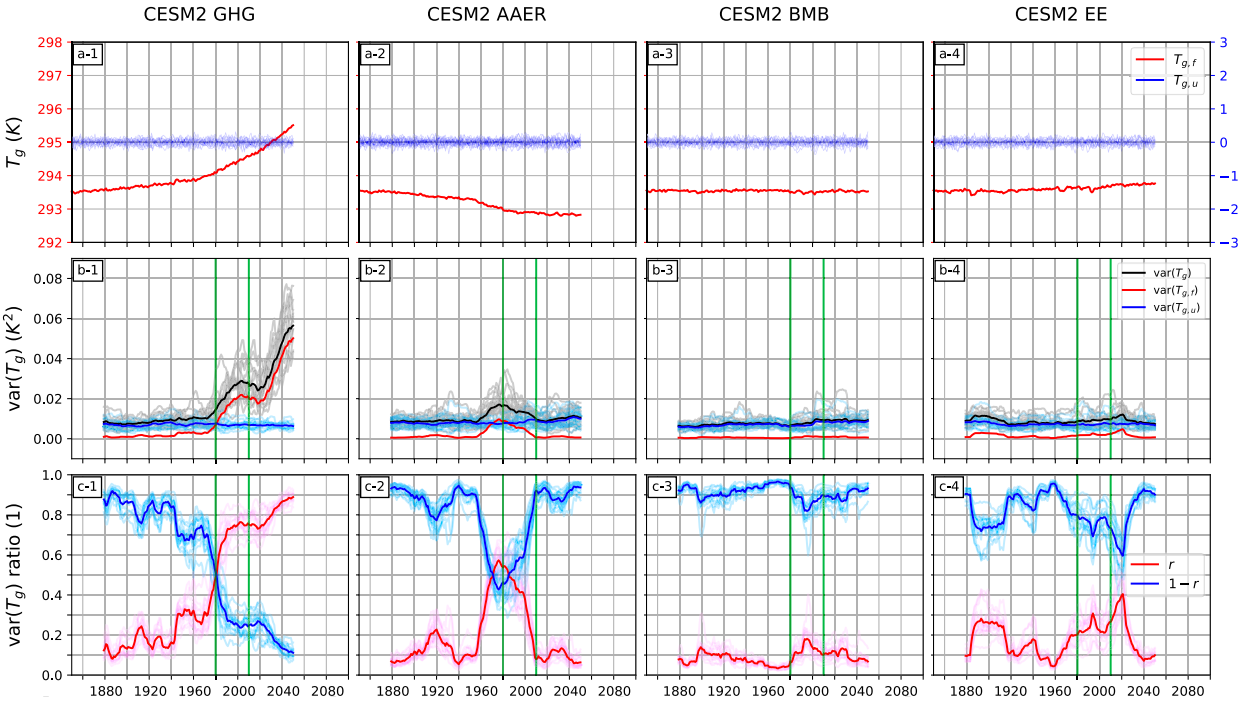

FIG. 6. As in Fig. 1, but for each CESM2 single-forcing experiment. (a) Time evolution of forced (red; y axis on the left) and unforced (blue; y axis on the right) T_g in CESM2 [a(1)] GHGs, [a(2)] AAERs, [a(3)] BMBs, and [a(4)] EE evolving simulations. (b) Time evolution of the variance of T_g (black), $T_{g,f}$ (red), and $T_{g,u}$ (blue) in each single-forcing ensemble. (c) The ratio of the $T_{g,f}$ variance [red; r defined in Eq. (1.12)] and the ratio of the $T_{g,u}$ variance [blue; $(1-r)$] in each single-forcing large ensembles. Note that the x axis marks the year in (a), while it denotes the end year of 30-yr moving windows in (b) and (c). For each panel, dark-colored lines indicate the ensemble mean and light-colored lines show each ensemble member. The two vertical green lines in (b) and (c) mark the end years of 1980 and 2010, which respectively indicate the results from 1951–80 and 1981–2010 windows that we focus on.

5. Impacts of individual forcing agents

a. *Single-forcing large ensembles*

In previous sections, we separate the forced and unforced components of SST/EIS patterns and the corresponding low-cloud feedback through initial-condition large ensembles. We also highlight the increasing importance of the forced component in modulating low-cloud feedback over the past few decades. The forced component is induced by the full historical and future radiative forcing that comprises different forcing agents. Previous studies have suggested that varying combinations of forcing agents can lead to changes in radiative feedbacks (Marvel et al. 2016; Gregory et al. 2020; Günther et al. 2022; Salvi et al. 2023; Zhou et al. 2023). Here, we place additional emphasis on understanding how the various forcing agents contribute to the relative importance of the forced and unforced components shown in the preceding sections. Specifically, we ask whether different combinations of forcing agents would shift the crossover time of forced responses compared to unforced variations.

To address the question, we leverage single-forcing large ensembles in several AOGCMs, where each simulation is perturbed with a specific type of forcing evolving over time. Forcing types other than the designated forcing are held fixed, allowing for isolating the impacts of individual forcings. For example, CESM2 single-forcing large ensembles (Simpson et al. 2023) include simulations where only "GHG," or anthropogenic aerosols ("AAER"), or biomass burning aerosols ("BMB") evolve, and simulations where all other forcings evolve except for GHG, AAER, or BMB (everything else evolving or "EE"; Table S2). In addition to CESM2, we investigate four other single-forcing large ensembles that participated in the Detection and Attribution Model Intercomparison Project (DAMIP; Ribes et al. 2015; Gillett et al. 2016), namely, CanESM5, GISS-E2.1-G, HadGEM3-GC3.1-LL, and MIROC6. In DAMIP, single-forcing experiments include simulations where only greenhouse gases ("hist-GHG"), or aerosols ("hist-aer"), or natural forcings evolve (such as solar and volcanic forcings; "hist-nat"). We selected models with at least 10 ensembles for each single-forcing experiment and at least 40 ensembles for the all-forcing simulation at the time of analysis. An exception is our in-house model GISS-E2.1-G, which has only five members in the AAER simulation (Table S3). Note that the aerosol forcing in DAMIP hist-aer includes both anthropogenic and biomass-burning aerosols, while the two are separated in CESM2 single-forcing large ensembles.

b. *Compensation between anthropogenic aerosols and greenhouse gases*

Figure 6 illustrates the forced and unforced T_g associated with each forcing agent in CESM2. The GHG-forced T_g shows a rising trend as expected [Fig. 6a(1)]. The variance of

GHG-forced T_g also increases over time, reflecting a stronger GHG-forced warming rate in late periods, especially for the 30-yr windows ending after the 1980s [Fig. 6b(1)]. On the other hand, anthropogenic-aerosol-forced T_g generally decreases over time, with a stronger decreasing trend from the 1950s to the 1980s [Fig. 6a(2)], corresponding to a local maximum of $T_{g,f}$ variance around the 30-yr window of 1951–80 [the first green line in Fig. 6b(2)]. Unlike the GHG and AAER simulations, the forced T_g in the BMB and EE simulations varies weakly throughout the historical period [Figs. 6a(3) and 6a(4)] and its forced T_g variance is consistently much weaker than the unforced T_g variance [Figs. 6b(3) and 6b(4)]. The forced T_g variance in the EE simulations exhibits slightly stronger temporal variation that highlights the global-mean cooling from historical volcanic eruptions [Fig. 6b(4), as discussed in section 2d].

Figure 6c shows the relative importance of forced regressions [expressed as r; Eq. (1.12)] and unforced regressions ($1 - r$) across various single-forcing experiments. Within these single-forcing ensembles, the time evolution of r in GHG-only ensembles shows a resemblance to those in large ensembles where all forcings are time-dependent. Such similarity suggests that the growing importance of forced responses in all-forcing large ensembles is primarily due to emissions of GHGs. Furthermore, we emphasize that the transition from a domination of unforced regressions ($r < 0.5$) to a domination of forced regressions ($r > 0.5$) occurs about 20 years earlier in GHG-only ensembles than in all-forcing ensembles. The transition period is around the 1951–80 window in GHG-only ensembles [Fig. 6c(1)] and around the 1971–2000 window in all-forcing ensembles (Fig. 1g).

The delayed transition in all-forcing ensembles can be understood through the compensating effect on global-mean temperatures between anthropogenic aerosols and greenhouse gases forcings (Deser et al. 2020), which is particularly pronounced from the 1950s to the 1980s. During this time, the global-mean cooling induced by anthropogenic aerosols partially offsets the global-mean warming from greenhouse gases (compare $T_{g,f}$ time evolution in Fig. 6a), leading to weaker warming in all-forcing ensembles. In the absence of such compensation, the GHG-forced warming would have outweighed the unforced temperature variation starting from the 30-yr window of 1951–80 [Fig. 6c(1)]. The aerosol-forced cooling trends weaken post-1980s, corresponding to the overall maximum of r around the 1951–80 window [Fig. 6c(2)]. In turn, this implies that aerosol forcing has potentially delayed the transition to a more-negative low-cloud feedback by masking GHG-forced warming.

Despite our main focus on CESM2, we highlight that multiple AOGCMs agree on the 10–20 years of shift in forced temperature domination between all-forcing large ensembles and GHG-only experiments (Fig. 7). For example, the crossover of $r > 0.5$ in CanESM5 all-forcing ensembles occurs around the 1951–80 window (Fig. 7a), which is about 10 years later compared to GHG-only ensembles (1941–70 window; Fig. 7b). In GISS-E2.1-G, the crossover occurs around the 1971–2000 window (Fig. 7e, identical to Fig. 1i), which is about 20 years later than in GHG-only ensembles (1951–80 window; Fig. 7f). In HadGEM3-GC3.1-LL, the crossover happens around the 1961–90 window (Fig. 7i), about 20 years later compared to GHG-only ensembles (1941–70 window; Fig. 7j). Last, in MIROC6, the unforced temperature variance is much stronger than the forced temperature variance throughout the historical period, and the crossover of forced variance barely happens within the historical period (Fig. 7m).

When interpreting results from single-forcing large ensembles, it is important to note potential nonlinearities, where the responses from individual forcings may not sum to the all-forcing responses (Simpson et al. 2023). This nonlinearity could introduce uncertainty in assessing the relative strength of each forcing agent in shaping the time evolution of radiative feedbacks. Also, while we focus on the compensating effect between GHG-forced and aerosol-forced T_g and its implications for the relative contributions of forced and unforced feedbacks, it is important to note that the SST spatial patterns resulting from each forcing can differ significantly (Salvi et al. 2023). These differences in forced SST patterns can influence the time evolution of forced feedback through the pattern effect, as discussed in detail in section 4.

6. Summary and discussion

This research examines the role of the SST pattern effect in driving the time-varying low-cloud feedback (C), with a particular focus on the relative importance between forced responses and unforced variability. We provide evidence that the time variation of C estimated via OLS regressions can be attributed to three main contributors: changes in its forced component, changes in its unforced component, and changes in the relative importance between the forced and unforced components (see sections 2c and 3c for more details).

Using initial-condition large ensembles, we find that the unforced signals outweigh the forced signals for 30-yr windows ending prior to the 1980s (Figs. 1g–i and 7a,e,i,m); thus, the overall SST and EIS patterns are strongly influenced by the unforced components, characterizing ENSO-like surface conditions (Figs. 4 and 5). For 30-yr windows ending after the 1980s, the forced signals have strengthened, surpassing unforced signals around 30-yr windows ending between the 2000s and the 2010s (Figs. 1g–i and 7a,e,i,m). The transition time toward the domination of forced components involves the compensation on global-mean temperatures from greenhouse gases and aerosols. If only greenhouse gases are time-evolving, the transition time would occur 10–20 years earlier than in the all-forcing simulations (compare r in Figs. 1, 6, and 7). Since the forced SST patterns are relatively uniform (the second column of Fig. 4), the overall SST patterns after the 1980s have become less heterogeneous (the first column of Fig. 4). The time-evolving SST pattern gives rise to changes in low-cloud feedback C_{SST} directly and through modifying low-level stability (C_{EIS}). The terms C_{SST} and C_{EIS} are the low-cloud radiative feedbacks due to changes in SST and EIS, respectively. Most of the ensemble members in CESM2 and MPI-ESM1.1 agree on the stabilizing shift of C_{EIS} in the recent 30–50 years, with a magnitude larger than the change in C_{SST}. More importantly, we find that the increasing importance of forced signals is the dominant contributor to the negative shift of C_{EIS} over the past few decades within climate models (Fig. 2). These results suggest that a similar

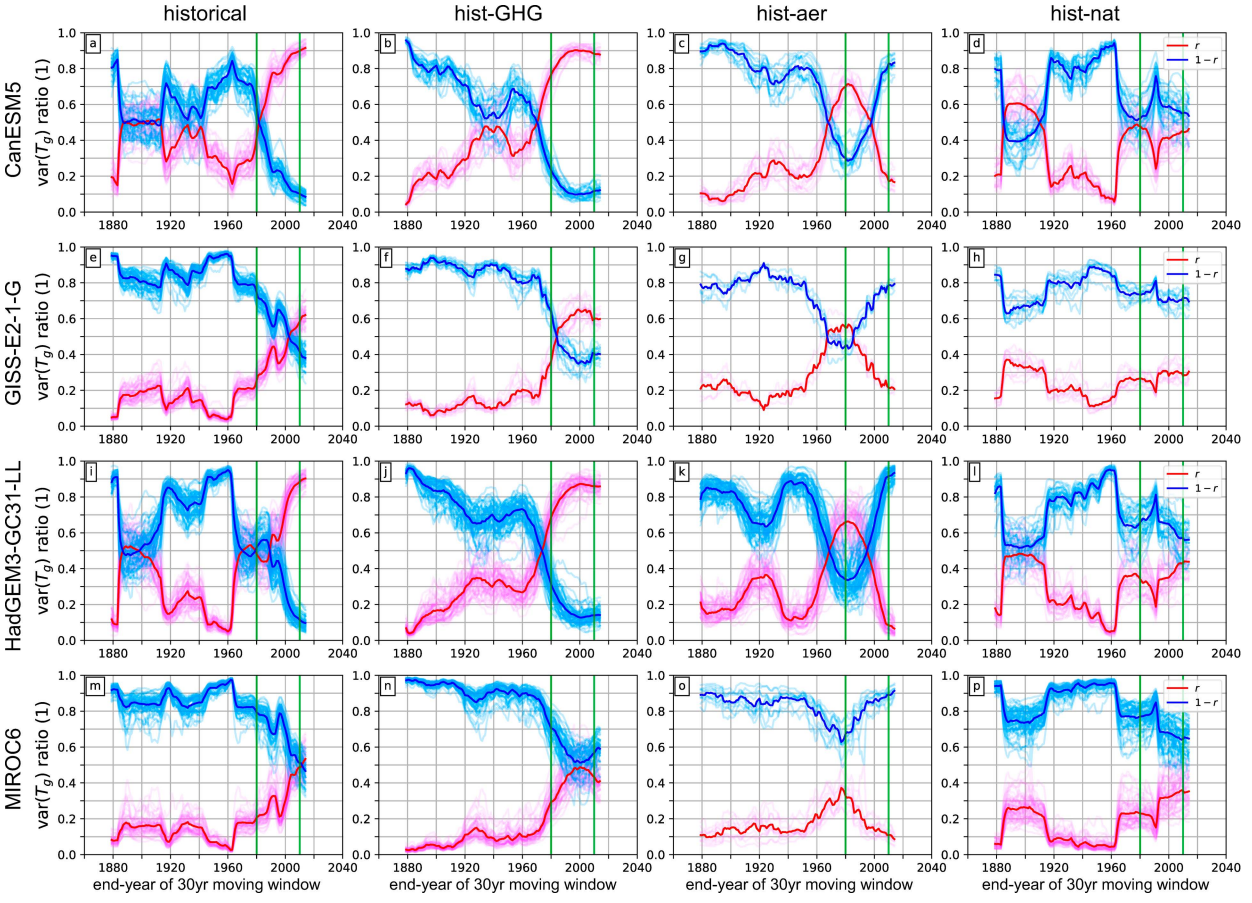

FIG. 7. Relative importance of the forced regressions r (red) and unforced regressions $[(1 - r)$; blue] in (a) all-forcing LEs, (b) hist-GHG, (c) hist-aer, and (d) hist-nat experiments in CanESM5. Other rows are as in (a)–(d), but for (e)–(h) GISS-E2.1-G, (i)–(l) HadGEM3-GC3.1-LL, and (m)–(p) MIROC6. Dark-colored lines show the ensemble mean, and light-colored lines show individual ensemble members. (e) As in Fig. 1i.

transition toward an increasing importance of the forced signal may have contributed to the negative shift in C_{EIS} in observations as well.

The research highlights the crucial role of strengthening forced responses relative to unforced variations in modifying low-cloud feedback, especially within recent decades when the overall radiative feedback shifts from being dominated by unforced signals to being dominated by forced signals. This shift can lead to large apparent time variations in feedbacks that are distinct from the type of pattern-effect mechanisms related to ocean heat uptake that are invoked to explain time-varying feedbacks in CO_2 doubling or quadrupling simulations. Rather, the time-evolving pattern described here arises from the fact that OLS estimates have a time-varying mix of forced and unforced SST patterns and feedbacks. Thus, a "pattern effect" may arise even if both forced and unforced patterns are themselves time-invariant. Therefore, we suggest that the forced and unforced components of the radiative feedbacks should be evaluated separately.

Acknowledgments. We thank three reviewers, Timothy Andrews and two anonymous reviewers, for their constructive comments. The work of Y.-J. L., G. V. C., C. P., and K. C. A. was supported by the U.S. Department of Energy (DOE) Regional and Global Model Analysis program Grant DE-SC0022110. The work of M. D. Z. was supported by the U.S. DOE Regional and Global Model Analysis program area and was performed under the auspices of the U.S. DOE by Lawrence Livermore National Laboratory under Contract DE-AC52-07NA27344. K. C. A. was supported by the National Science Foundation (NSF) Award AGS-1752796, the National Oceanic and Atmospheric Administration (NOAA) MAPP Program Award NA20OAR4310391, and a Calvin Professorship in Oceanography.

Data availability statement. The CESM2 large ensemble dataset was made available by the CESM2 Large Ensemble Community Project and supercomputing resources from the IBS Center for Climate Physics in South Korea, which can be downloaded from https://www.cesm.ucar.edu/community-projects/lens2/data-sets. The CESM2 single-forcing large ensemble data can be downloaded from the NCAR Climate Data Gateway (https://www.earthsystemgrid.org/dataset/ucar.cgd.cesm2.single.forcing.large.ensemble.html). The large ensemble

data from the Max Planck Institute for Meteorology can be downloaded from https://www.mpimet.mpg.de/en/grand-ensemble/. The large ensemble data from other models used in this study (including GISS-E2.1-G, CanESM5, HadGEM3-GC3.1-LL, and MIROC6) can be downloaded from the ESGF portal (https://esgf-node.llnl.gov/search/cmip6/). The meteorological cloud radiative kernels were developed by Scott et al. (2020) and can be downloaded from https://github.com/tamyers87/meteorological_cloud_radiative_kernels.

REFERENCES

Andrews, T., and M. J. Webb, 2018: The dependence of global cloud and lapse rate feedbacks on the spatial structure of tropical Pacific warming. *J. Climate*, **31**, 641–654, https://doi.org/10.1175/JCLI-D-17-0087.1.

——, J. M. Gregory, and M. J. Webb, 2015: The dependence of radiative forcing and feedback on evolving patterns of surface temperature change in climate models. *J. Climate*, **28**, 1630–1648, https://doi.org/10.1175/JCLI-D-14-00545.1.

——, and Coauthors, 2018: Accounting for changing temperature patterns increases historical estimates of climate sensitivity. *Geophys. Res. Lett.*, **45**, 8490–8499, https://doi.org/10.1029/2018GL078887.

——, and Coauthors, 2022: On the effect of historical SST patterns on radiative feedback. *J. Geophys. Res. Atmos.*, **127**, e2022JD036675, https://doi.org/10.1029/2022JD036675.

Armour, K. C., C. M. Bitz, and G. H. Roe, 2013: Time-varying climate sensitivity from regional feedbacks. *J. Climate*, **26**, 4518–4534, https://doi.org/10.1175/JCLI-D-12-00544.1.

——, and Coauthors, 2024: Sea-surface temperature pattern effects have slowed global warming and biased warming-based constraints on climate sensitivity. *Proc. Natl. Acad. Sci. USA*, **121**, e2312093121, https://doi.org/10.1073/pnas.2312093121.

Bauer, S. E., and Coauthors, 2020: Historical (1850–2014) aerosol evolution and role on climate forcing using the GISS ModelE2.1 contribution to CMIP6. *J. Adv. Model. Earth Syst.*, **12**, e2019MS001978, https://doi.org/10.1029/2019MS001978.

Bony, S., and J.-L. Dufresne, 2005: Marine boundary layer clouds at the heart of tropical cloud feedback uncertainties in climate models. *Geophys. Res. Lett.*, **32**, L20806, https://doi.org/10.1029/2005GL023851.

Caldwell, P. M., M. D. Zelinka, K. E. Taylor, and K. Marvel, 2016: Quantifying the sources of intermodel spread in equilibrium climate sensitivity. *J. Climate*, **29**, 513–524, https://doi.org/10.1175/JCLI-D-15-0352.1.

Ceppi, P., and J. M. Gregory, 2017: Relationship of tropospheric stability to climate sensitivity and Earth's observed radiation budget. *Proc. Natl. Acad. Sci. USA*, **114**, 13 126–13 131, https://doi.org/10.1073/pnas.1714308114.

——, and ——, 2019: A refined model for the Earth's global energy balance. *Climate Dyn.*, **53**, 4781–4797, https://doi.org/10.1007/s00382-019-04825-x.

Deser, C., and Coauthors, 2020: Isolating the evolving contributions of anthropogenic aerosols and greenhouse gases: A new CESM1 large ensemble community resource. *J. Climate*, **33**, 7835–7858, https://doi.org/10.1175/JCLI-D-20-0123.1.

Dessler, A. E., 2020: Potential problems measuring climate sensitivity from the historical record. *J. Climate*, **33**, 2237–2248, https://doi.org/10.1175/JCLI-D-19-0476.1.

——, T. Mauritsen, and B. Stevens, 2018: The influence of internal variability on Earth's energy balance framework and implications for estimating climate sensitivity. *Atmos. Chem. Phys.*, **18**, 5147–5155, https://doi.org/10.5194/acp-18-5147-2018.

Dong, Y., C. Proistosescu, K. C. Armour, and D. S. Battisti, 2019: Attributing historical and future evolution of radiative feedbacks to regional warming patterns using a Green's function approach: The preeminence of the western Pacific. *J. Climate*, **32**, 5471–5491, https://doi.org/10.1175/JCLI-D-18-0843.1.

——, K. C. Armour, M. D. Zelinka, C. Proistosescu, D. S. Battisti, C. Zhou, and T. Andrews, 2020: Intermodel spread in the pattern effect and its contribution to climate sensitivity in CMIP5 and CMIP6 models. *J. Climate*, **33**, 7755–7775, https://doi.org/10.1175/JCLI-D-19-1011.1.

——, and Coauthors, 2021: Biased estimates of equilibrium climate sensitivity and transient climate response derived from historical CMIP6 simulations. *Geophys. Res. Lett.*, **48**, e2021GL095778, https://doi.org/10.1029/2021GL095778.

——, A. G. Pauling, S. Sadai, and K. C. Armour, 2022: Antarctic ice-sheet meltwater reduces transient warming and climate sensitivity through the sea-surface temperature pattern effect. *Geophys. Res. Lett.*, **49**, e2022GL101249, https://doi.org/10.1029/2022GL101249.

Donohoe, A., K. C. Armour, A. G. Pendergrass, and D. S. Battisti, 2014: Shortwave and longwave radiative contributions to global warming under increasing CO_2. *Proc. Natl. Acad. Sci. USA*, **111**, 16 700–16 705, https://doi.org/10.1073/pnas.1412190111.

Eiselt, K.-U., and R. G. Graversen, 2023: On the control of Northern Hemispheric feedbacks by AMOC: Evidence from CMIP and slab ocean modeling. *J. Climate*, **36**, 6777–6795, https://doi.org/10.1175/JCLI-D-22-0884.1.

Eitzen, Z. A., W. Su, K.-M. Xu, N. Loeb, M. Sun, D. Doelling, F. Rose, and A. Bodas-Salcedo, 2017: Evaluation of a general circulation model by the CERES flux-by-cloud type simulator. *J. Geophys. Res. Atmos.*, **122**, 10 655–10 668, https://doi.org/10.1002/2017JD027076.

Forster, P., and Coauthors, 2021: The Earth's energy budget, climate feedbacks, and climate sensitivity. *Climate Change 2021: The Physical Science Basis*, V. Masson-Delmotte et al., Eds., Cambridge University Press, 923–1054, https://doi.org/10.1017/9781009157896.009.

Frey, W. R., E. A. Maroon, A. G. Pendergrass, and J. E. Kay, 2017: Do Southern Ocean cloud feedbacks matter for 21st century warming? *Geophys. Res. Lett.*, **44**, 12 447–12 456, https://doi.org/10.1002/2017GL076339.

Geoffroy, O., D. Saint-Martin, G. Bellon, A. Voldoire, D. Olivié, and S. Tytéca, 2013: Transient climate response in a two-layer energy-balance model. Part II: Representation of the efficacy of deep-ocean heat uptake and validation for CMIP5 AOGCMs. *J. Climate*, **26**, 1859–1876, https://doi.org/10.1175/JCLI-D-12-00196.1.

Gillett, N. P., and Coauthors, 2016: The Detection and Attribution Model Intercomparison Project (DAMIP v1.0) contribution to CMIP6. *Geosci. Model Dev.*, **9**, 3685–3697, https://doi.org/10.5194/gmd-9-3685-2016.

Gjermundsen, A., A. Nummelin, D. Olivié, M. Bentsen, Ø. Seland, and M. Schulz, 2021: Shutdown of Southern Ocean convection controls long-term greenhouse gas-induced warming. *Nat. Geosci.*, **14**, 724–731, https://doi.org/10.1038/s41561-021-00825-x.

Gregory, J. M., and T. Andrews, 2016: Variation in climate sensitivity and feedback parameters during the historical period. *Geophys. Res. Lett.*, **43**, 3911–3920, https://doi.org/10.1002/2016GL068406.

——, R. J. Stouffer, S. C. B. Raper, P. A. Stott, and N. A. Rayner, 2002: An observationally based estimate of the climate sensitivity. *J. Climate*, **15**, 3117–3121, https://doi.org/10.1175/1520-0442(2002)015<3117:AOBEOT>2.0.CO;2.

——, and Coauthors, 2004: A new method for diagnosing radiative forcing and climate sensitivity. *Geophys. Res. Lett.*, **31**, L03205, https://doi.org/10.1029/2003GL018747.

——, T. Andrews, P. Good, T. Mauritsen, and P. M. Forster, 2016: Small global-mean cooling due to volcanic radiative forcing. *Climate Dyn.*, **47**, 3979–3991, https://doi.org/10.1007/s00382-016-3055-1.

——, ——, P. Ceppi, T. Mauritsen, and M. Webb, 2020: How accurately can the climate sensitivity to CO_2 be estimated from historical climate change? *Climate Dyn.*, **54**, 129–157, https://doi.org/10.1007/s00382-019-04991-y.

Günther, M., H. Schmidt, C. Timmreck, and M. Toohey, 2022: Climate feedback to stratospheric aerosol forcing: The key role of the pattern effect. *J. Climate*, **35**, 7903–7917, https://doi.org/10.1175/JCLI-D-22-0306.1.

Heidinger, A. K., M. J. Foster, A. Walther, and X. T. Zhao, 2014: The pathfinder atmospheres–extended AVHRR climate dataset. *Bull. Amer. Meteor. Soc.*, **95**, 909–922, https://doi.org/10.1175/BAMS-D-12-00246.1.

Held, I. M., M. Winton, K. Takahashi, T. Delworth, F. Zeng, and G. K. Vallis, 2010: Probing the fast and slow components of global warming by returning abruptly to preindustrial forcing. *J. Climate*, **23**, 2418–2427, https://doi.org/10.1175/2009JCLI3466.1.

Huber, M., U. Beyerle, and R. Knutti, 2014: Estimating climate sensitivity and future temperature in the presence of natural climate variability. *Geophys. Res. Lett.*, **41**, 2086–2092, https://doi.org/10.1002/2013GL058532.

Kelley, M., and Coauthors, 2020: GISS-E2.1: Configurations and climatology. *J. Adv. Model. Earth Syst.*, **12**, e2019MS002025, https://doi.org/10.1029/2019MS002025.

Lin, Y.-J., Y.-T. Hwang, P. Ceppi, and J. M. Gregory, 2019: Uncertainty in the evolution of climate feedback traced to the strength of the Atlantic Meridional Overturning Circulation. *Geophys. Res. Lett.*, **46**, 12 331–12 339, https://doi.org/10.1029/2019GL083084.

——, ——, J. Lu, F. Liu, and B. E. J. Rose, 2021: The dominant contribution of Southern Ocean heat uptake to time-evolving radiative feedback in CESM. *Geophys. Res. Lett.*, **48**, e2021GL093302, https://doi.org/10.1029/2021GL093302.

Maher, N., and Coauthors, 2019: The Max Planck Institute Grand Ensemble: Enabling the exploration of climate system variability. *J. Adv. Model. Earth Syst.*, **11**, 2050–2069, https://doi.org/10.1029/2019MS001639.

Marvel, K., G. A. Schmidt, R. L. Miller, and L. S. Nazarenko, 2016: Implications for climate sensitivity from the response to individual forcings. *Nat. Climate Change*, **6**, 386–389, https://doi.org/10.1038/nclimate2888.

Mauritsen, T., 2016: Clouds cooled the Earth. *Nat. Geosci.*, **9**, 865–867, https://doi.org/10.1038/ngeo2838.

Miller, R. L., and Coauthors, 2021: CMIP6 historical simulations (1850–2014) with GISS-E2.1. *J. Adv. Model. Earth Syst.*, **13**, e2019MS002034, https://doi.org/10.1029/2019MS002034.

Myers, T. A., R. C. Scott, M. D. Zelinka, S. A. Klein, J. R. Norris, and P. M. Caldwell, 2021: Observational constraints on low cloud feedback reduce uncertainty of climate sensitivity. *Nat. Climate Change*, **11**, 501–507, https://doi.org/10.1038/s41558-021-01039-0.

Pincus, R., P. M. Forster, and B. Stevens, 2016: The Radiative Forcing Model Intercomparison Project (RFMIP): Experimental protocol for CMIP6. *Geosci. Model Dev.*, **9**, 3447–3460, https://doi.org/10.5194/gmd-9-3447-2016.

Platnick, S., and Coauthors, 2015: MODIS cloud optical properties: User guide for the collection 6 level-2 MOD06/MYD06 product and associated level-3 datasets, version 1.0. MODIS Tech. Doc., 145 pp., https://modis-images.gsfc.nasa.gov/_docs/C6MOD06OPUserGuide.pdf.

Proistosescu, C., A. Donohoe, K. C. Armour, G. H. Roe, M. F. Stuecker, and C. M. Bitz, 2018: Radiative feedbacks from stochastic variability in surface temperature and radiative imbalance. *Geophys. Res. Lett.*, **45**, 5082–5094, https://doi.org/10.1029/2018GL077678.

Ribes, A., N. P. Gillett, and F. W. Zwiers, 2015: Designing detection and attribution simulations for CMIP6 to optimize the estimation of greenhouse gas–induced warming. *J. Climate*, **28**, 3435–3438, https://doi.org/10.1175/JCLI-D-14-00691.1.

Rodgers, K. B., and Coauthors, 2021: Ubiquity of human-induced changes in climate variability. *Earth Syst. Dyn.*, **12**, 1393–1411, https://doi.org/10.5194/esd-12-1393-2021.

Rose, B. E. J., and L. Rayborn, 2016: The effects of ocean heat uptake on transient climate sensitivity. *Curr. Climate Change Rep.*, **2**, 190–201, https://doi.org/10.1007/s40641-016-0048-4.

——, K. C. Armour, D. S. Battisti, N. Feldl, and D. D. B. Koll, 2014: The dependence of transient climate sensitivity and radiative feedbacks on the spatial pattern of ocean heat uptake. *Geophys. Res. Lett.*, **41**, 1071–1078, https://doi.org/10.1002/2013GL058955.

Rugenstein, M., and Coauthors, 2020: Equilibrium climate sensitivity estimated by equilibrating climate models. *Geophys. Res. Lett.*, **47**, e2019GL083898, https://doi.org/10.1029/2019GL083898.

Rugenstein, M. A. A., and K. C. Armour, 2021: Three flavors of radiative feedbacks and their implications for estimating equilibrium climate sensitivity. *Geophys. Res. Lett.*, **48**, e2021GL092983, https://doi.org/10.1029/2021GL092983.

——, K. Caldeira, and R. Knutti, 2016: Dependence of global radiative feedbacks on evolving patterns of surface heat fluxes. *Geophys. Res. Lett.*, **43**, 9877–9885, https://doi.org/10.1002/2016GL070907.

Salvi, P., J. M. Gregory, and P. Ceppi, 2023: Time-evolving radiative feedbacks in the historical period. *J. Geophys. Res. Atmos.*, **128**, e2023JD038984, https://doi.org/10.1029/2023JD038984.

Scott, R. C., T. A. Myers, J. R. Norris, M. D. Zelinka, S. A. Klein, M. Sun, and D. R. Doelling, 2020: Observed sensitivity of low-cloud radiative effects to meteorological perturbations over the global oceans. *J. Climate*, **33**, 7717–7734, https://doi.org/10.1175/JCLI-D-19-1028.1.

Sherwood, S. C., S. Bony, and J.-L. Dufresne, 2014: Spread in model climate sensitivity traced to atmospheric convective mixing. *Nature*, **505**, 37–42, https://doi.org/10.1038/nature12829.

——, and Coauthors, 2020: An assessment of Earth's climate sensitivity using multiple lines of evidence. *Rev. Geophys.*, **58**, e2019RG000678, https://doi.org/10.1029/2019RG000678.

Shindell, D. T., 2014: Inhomogeneous forcing and transient climate sensitivity. *Nat. Climate Change*, **4**, 274–277, https://doi.org/10.1038/nclimate2136.

Simpson, I. R., and Coauthors, 2023: The CESM2 single-forcing large ensemble and comparison to CESM1: Implications for experimental design. *J. Climate*, **36**, 5687–5711, https://doi.org/10.1175/JCLI-D-22-0666.1.

Stevens, B., S. C. Sherwood, S. Bony, and M. J. Webb, 2016: Prospects for narrowing bounds on Earth's equilibrium climate sensitivity. *Earth's Future*, **4**, 512–522, https://doi.org/10.1002/2016EF000376.

Uribe, A., F. A.-M. Bender, and T. Mauritsen, 2022: Observed and CMIP6 modeled internal variability feedbacks and their relation to forced climate feedbacks. *Geophys. Res. Lett.*, **49**, e2022GL100075, https://doi.org/10.1029/2022GL100075.

Watanabe, M., J.-L. Dufresne, Y. Kosaka, T. Mauritsen, and H. Tatebe, 2021: Enhanced warming constrained by past trends in equatorial Pacific sea surface temperature gradient. *Nat. Climate Change*, **11**, 33–37, https://doi.org/10.1038/s41558-020-00933-3.

Wills, R. C. J., K. C. Armour, D. S. Battisti, C. Proistosescu, and L. A. Parsons, 2021: Slow modes of global temperature variability and their impact on climate sensitivity estimates. *J. Climate*, **34**, 8717–8738, https://doi.org/10.1175/JCLI-D-20-1013.1.

——, Y. Dong, C. Proistosecu, K. C. Armour, and D. S. Battisti, 2022: Systematic climate model biases in the large-scale patterns of recent sea-surface temperature and sea-level pressure change. *Geophys. Res. Lett.*, **49**, e2022GL100011, https://doi.org/10.1029/2022GL100011.

Winton, M., K. Takahashi, and I. M. Held, 2010: Importance of ocean heat uptake efficacy to transient climate change. *J. Climate*, **23**, 2333–2344, https://doi.org/10.1175/2009JCLI3139.1.

Wood, R., and C. S. Bretherton, 2006: On the relationship between stratiform low cloud cover and lower-tropospheric stability. *J. Climate*, **19**, 6425–6432, https://doi.org/10.1175/JCLI3988.1.

Xie, S.-P., Y. Kosaka, and Y. M. Okumura, 2016: Distinct energy budgets for anthropogenic and natural changes during global warming hiatus. *Nat. Geosci.*, **9**, 29–33, https://doi.org/10.1038/ngeo2581.

Young, A. H., K. R. Knapp, A. Inamdar, W. Hankins, and W. B. Rossow, 2018: The International Satellite Cloud Climatology Project H-Series climate data record product. *Earth Syst. Sci. Data*, **10**, 583–593, https://doi.org/10.5194/essd-10-583-2018.

Zelinka, M. D., C. Zhou, and S. A. Klein, 2016: Insights from a refined decomposition of cloud feedbacks. *Geophys. Res. Lett.*, **43**, 9259–9269, https://doi.org/10.1002/2016GL069917.

Zhou, C., M. D. Zelinka, and S. A. Klein, 2016: Impact of decadal cloud variations on the Earth's energy budget. *Nat. Geosci.*, **9**, 871–874, https://doi.org/10.1038/ngeo2828.

——, ——, and ——, 2017: Analyzing the dependence of global cloud feedback on the spatial pattern of sea surface temperature change with a Green's function approach. *J. Adv. Model. Earth Syst.*, **9**, 2174–2189, https://doi.org/10.1002/2017MS001096.

——, M. Wang, M. D. Zelinka, Y. Liu, Y. Dong, and K. C. Armour, 2023: Explaining forcing efficacy with pattern effect and state dependence. *Geophys. Res. Lett.*, **50**, e2022GL101700, https://doi.org/10.1029/2022GL101700.